Elsevier Editorial System(tm) for Lithos
Manuscript Draft

Corresponding Author: Prof. Sergio Rocchi,

Corresponding Author's Institution: Università di Pisa

First Author: Sergio Rocchi, Prof.

Order of Authors: Sergio Rocchi, Prof.; Gianfranco Di Vincenzo, Dr.; Andrea Dini, Dr.; Maurizio Petrelli, Dr.; Simone Vezzoni, Dr.

Abstract: Growth of continental crust in accretionary orogenic belts takes place through repeated cycles of subduction-accretion of rock units from continental and oceanic magmatic arcs, supra-subduction zone backarcs and forearcs loaded with continent-derived materials. An ancient example relevant to magmatic arc accretion models is represented by the remnants of the Cambrian-Ordovician Ross Orogen in the Morozumi Range, Victoria Land (Antarctica). There, late Neoproterozoic phyllites host an intrusive complex which preserves a remarkably uncommon record of genetically unrelated magma pulses emplaced under a variable stress regime in a short time span: (1) a dominant K-feldspar-phyric granite, (2) fine-grained dioritic stocks and dykes, (3) a peraluminous granite; (4) a tonalitic-granodioritic dyke swarm. Laserprobe U-Pb zircon dates cluster at late Cambrian times for all these units, yet they carry differential cargoes of relict cores. Unique geochemical-isotopic signatures for both the less evolved magmas (diorite and dyke tonalite) and the most acidic ones (granite and peraluminous granite) indicate that each one of them originated from distinct sources at depth. Additionally, field relationships and chemical evolutionary trends testify for a variety of shallow level open-system processes, such as magma mingling/mixing between diorite and main granite magmas, as well as progressive incorporation of the host schists by the dyke tonalite magma. In summary, crustal growth in the Morozumi intrusive complex was contributed by fresh mantle magma issuing from the metasomatized mantle wedge, while the production of other melts did recycle different crustal portions/layers: the main granite derived from Grenville-age granulitic lower crust; the peraluminous granite from late Proterozoic upper crust; the tonalite magmas derived from subduction erosion-enriched subarc mantle and evolved by ingestion of local metasedimentary rocks. Overall, the Morozumi intrusive complex yields evidence for emplacement in the same site at the same time of magmas issuing from different sources that are usually found at different depth in the arc lithospheric section. A likely scenario to activate this specific mechanism of melt production is a subduction zone affected by subduction erosion.

1 **Time-space focused intrusion of genetically unrelated arc magmas**

2 **in the early Paleozoic Ross-Delamerian Orogen (Morozumi Range, Antarctica)**

3

4 S. Rocchi[1], G. Di Vincenzo[2], A. Dini[2], M. Petrelli[3], S. Vezzoni[1]

5

6 *1. Dipartimento di Scienze della Terra , Università di Pisa, Italy - tel: +390502215710,*

7 *fax: +390502215800, email: sergio.rocchi@unipi.it*

8 *2. Istituto di Geoscienze e Georisorse, CNR, Pisa, Italy*

9 *3. Dipartimento di Fisica e Geologia, Università di Perugia, Italy*

10

11 ABSTRACT

12 Growth of continental crust in accretionary orogenic belts takes place through repeated cycles

13 of subduction–accretion of rock units from continental and oceanic magmatic arcs, supra-

14 subduction zone backarcs and forearcs loaded with continent-derived materials. An ancient

15 example relevant to magmatic arc accretion models is represented by the remnants of the

16 Cambrian-Ordovician Ross Orogen in the Morozumi Range, Victoria Land (Antarctica). There,

17 late Neoproterozoic phyllites host an intrusive complex which preserves a remarkably

18 uncommon record of genetically unrelated magma pulses emplaced under a variable stress

19 regime in a short time span: (1) a dominant K-feldspar-phyric granite, (2) fine-grained dioritic

20 stocks and dykes, (3) a peraluminous granite; (4) a tonalitic-granodioritic dyke swarm.

21 Laserprobe U-Pb zircon dates cluster at late Cambrian times for all these units, yet they carry

22 differential cargoes of relict cores. Unique geochemical-isotopic signatures for both the less

23 evolved magmas (diorite and dyke tonalite) and the most acidic ones (granite and

24 peraluminous granite) indicate that each one of them originated from distinct sources at depth.

25 Additionally, field relationships and chemical evolutionary trends testify for a variety of

shallow level open-system processes, such as magma mingling/mixing between diorite and main granite magmas, as well as progressive incorporation of the host schists by the dyke tonalite magma. In summary, crustal growth in the Morozumi intrusive complex was contributed by fresh mantle magma issuing from the metasomatized mantle wedge, while the production of other melts did recycle different crustal portions/layers: the main granite derived from Grenville-age granulitic lower crust; the peraluminous granite from late Proterozoic upper crust; the tonalite magmas derived from subduction erosion-enriched subarc mantle and evolved by ingestion of local metasedimentary rocks. Overall, the Morozumi intrusive complex yields evidence for emplacement in the same site at the same time of magmas issuing from different sources that are usually found at different depth in the arc lithospheric section. A likely scenario to activate this specific mechanism of melt production is a subduction zone affected by subduction erosion.

1. Introduction

Magma generation in convergent settings is usually from multiple sources, including the mantle wedge, the overriding plate, and the subducting slab as well. The overriding plate can contribute as either a contaminant of uprising magmas (Davidson et al., 2005) or a direct source of melts from the upper/lower crust (Brown, 2013), and the juvenile underplates as well (Rocchi et al., 2009). The subducting lithosphere can contribute by direct partial melting (Defant and Drummond, 1990), addition to the mantle wedge of a subduction component via aqueous fluids/hydrous melts (Pearce and Peate, 1995), as well as via more massive, bulky processes such as subduction erosion (von Huene et al., 2004) and subduction of continental

crust (Hacker et al., 2011). Actual arc magmas are thus the outcome of a bouquet of processes (Davidson et al., 2005), including source melting degree and regime (equilibrium/ disequilibrium), fractional crystallization, (possibly accompanied by assimilation), and hybridization between different magmas, from deep crustal to emplacement levels (Brown, 2013). In accretionary orogens, processes of mantle modifications can occcur every time subduction takes over slab rollback and backarc opening. This variety of materials and processes makes orogenic igneous complexes a rich source of information, yet difficult to disentangle.

A magmatic arc that underwent most of these petrogenetic processes in a convergent accretionary setting was active during the early Paleozoic at the paleo-Pacific margin of Gondwana in Antarctica. The Cenozoic uplift linked to the West Antarctic rift system led to prominent exposures of arc deep-seated terrains in clean outcrops. Among these, the Morozumi Range igneous complex in northern Victoria Land is made of a variety of intrusive rocks with well exposed mutual chronological, petrological and structural relationships. Field observations, coupled with chemical data, isotopic geochemistry and geochronology, led to the reconstruction of a scenario that shed light on potential modalities of magma formation and evolution in magmatic arcs. Additionally, new implications on the evolution of the Antarctic margin of Gondwana in Cambrian-Ordovician time are proposed to update current models.

2. Geological setting

Today's Transantarctic Mountains represent the roots of an orogen exposed on the shoulder of the Cretaceous–Cenozoic West Antarctic rift system (Rossetti et al., 2006a). The orogen dates back to Neoproterozoic-late Paleozoic times, when the large-scale subduction-related crustal accretion known as the Ross-Delamerian(-Tyennan) Orogeny occurred in the frame of

the convergence between Paleo-Pacific oceanic lithosphere and the Gondwana continental margin. Remnants of this orogen are now exposed along 3500 km of the Transantarctic Mountains, as well as in southeastern Australia, Tasmania and the South Island of New Zealand (Boger and Miller, 2004; Flöttmann et al., 1993; Foden et al., 2006; Gibson and Ireland, 1996; Glen, 2013; Stump, 1995).

The begininning of the Ross-Delamerian orogenic cycle, as recorded by the age of the oldest magmatism, has long been debated. A possible diachronous inception of magmatism has been postulated based on the ages of oldes igneous rocks of 514 Ma in Australia (Foden et al., 2006), of 540-520 Ma in Victoria Land (Allibone and Wysoczanski, 2002; Giacomini et al., 2007; Rocchi et al., 2004), and of around 550 Ma in central Transantarctic Mountains (Encarnación and Grunow, 1996), with detrital zircon ages and glacial clasts reaching 580-590 Ma (Goodge et al., 2012; Goodge et al., 2004). However, there is no robust evidence that the Ross Orogeny and subduction-related arc magmatism started before c. 540-530 Ma, and the diachronous starting of the orogenic cycle in Antarctica and Australia has recently been questioned (Gibson et al., 2011; Turner et al., 2009). Nevertheless, the age and geochemical patterns of intrusive rocks suggest oblique convergence along a tectonically segmented margin (Encarnación and Grunow, 1996; Goodge, 2002; Goodge et al., 2012; Goodge et al., 2004; Rocchi et al., 1998; Stump et al., 2006). The latest magmas emplaced in the Ross Orogen are about 480 Ma, and evidence for younger (460-440 Ma) amagmatic contractional tectonic activity in Victoria Land is likely related to the early stages of the formation of the Lachlan Fold Belt (Di Vincenzo et al., 2007), which is best developed in southeastern Australia (Glen et al., 2007).

A key segment of the Transantarctic Mountains is their Pacific Ocean-Ross Sea termination in northern Victoria Land (Fig. 1), commonly considered the along-strike continuation of Australia in Antarctica (Finn et al., 1999; Flöttmann et al., 1993; Stump et al., 1986) and described as an assembly of three fault-bounded terranes (Bradshaw et al., 1985; Gibson and Wright, 1985; Kleinschmidt and Tessensohn, 1987; Stump et al., 1983; Weaver et al., 1984), namely, from the continent toward the ocean: (i) the metamorphic Wilson terrane intruded by

105   Cambrian-early Ordovician plutonic rocks (Bomparola et al., 2007; Rocchi et al., 1998; Stump,

106   1995), (ii) the volcanic-sedimentary Bowers terrane (Crispini et al., 2007; Weaver et al., 1984)

107   and (iii) the Robertson Bay terrane, with thick, weakly metamorphosed turbiditic sequences

108   intruded by Devonian granites (Di Vincenzo et al., 2014; GANOVEX TEAM, 1987; Rossetti et al.,

109   2006b).

110   Recent works (Bracciali et al., 2009; Federico et al., 2006; Ferraccioli et al., 2009; Ferraccioli

111   et al., 2002; Gemelli et al., 2009; Rocchi et al., 2003; Roland et al., 2004; Tessensohn and

112   Henjes-Kunst, 2005) led to an updated model of the Ross Orogeny in Victoria Land (Rocchi et

113   al., 2011). In this new Cambrian scenario, the convergent Paleo-Pacific margin of Gondwana

114   consisted of a main continuous subduction zone coupled with local, transient subduction zones

115   related to a more or less continuous ribbon of outboard pieces of stretched forearc regions.

116   Thus, the Victoria Land portion of the Ross orogenic belt is inferred to derive neither by

117   collision against the margin of large continents/exotic continental blocks, nor by the unique

118   accretion of forearc oceanic lithosphere. Rather, the transient coupling between the lower and

119   upper plates generated multiple docking of small-sized continental fragments with restricted

120   periods of co-existence of double subduction zones. The Ross Orogen in Victoria Land was thus

121   the result of alternate episodes of advancing and retreating subduction zone(s). Within the key

122   segment of Victoria Land, a critical area is thus represented by the boundary zone between the

123   Wilson arc and the forearc ribbon which underwent detachment and re-accretion to the arc

124   (Rocchi et al., 2011). Here, the intrusive complex of the Morozumi Range (Fig. 1) recorded

125   multiple episodes of magma emplacement in the same site, in a short time, under a variable

126   stress regime.

127

128   **3. The Morozumi Range intrusive complex - field and petrographic features**

129

130   The Morozumi Range intrusive complex is hosted by the Morozumi phyllites (Fig. 2a), a

metasedimentary unit with a late Neoproterozoic maximum deposition age, and characterised by a regionally extensive subvertical foliation, locally overprinted by contact metamorphic effects up to 600°C at 0.2 GPa [Engel, 1984 #2916]. The Morozumi phyllites are unconformably overlain by the Permian continental-fluvial sandstones of the Beacon Supergroup, which are in turn conformably overlain by the lava flows and intruded by the columnarly jointed sills of the early Jurassic Ferrar large igneous province. The intrusive complex consists of a set of magmatic bodies with variable composition and well exposed intrusive relationships (Fig. 2). Seven different intrusive units are defined in the field based on their petrographic features (see summary in Table 1).

Morozumi granite. The Morozumi granite is by far the largest intrusive unit of the complex, extending north-south for ca. 16 km, with an east-west width of 1 km to 6 km (Fig. 1). The contacts against the country rock are subvertical, so that the intrusion has the overall aspect of a subvertical large tabular body (Fig. 2a). It mostly consists of a porphyritic monzogranite with white to pink K-feldspar megacrysts (up to 5 cm, Fig. 2b) set in a medium-grained groundmass with 10-15 vol% red-brown biotite, and allanite as a common accessory phase. K-feldspar megacrysts locally define a subvertical igneous foliation and lineation, parallel to the host schist foliation.

Morozumi diorite. The southwesternmost part of the intrusive complex include mafic stocks and dykes intruding the Morozumi granite (Fig. 2m). The contact between the mafic and felsic units is either pillowing-sharp (Fig. 2n) or diffuse (Fig. 2h), suggesting coeval emplacement relationships. The Morozumi diorite is an equigranular, fine- to medium-grained quartz-diorite characterized by the occurrence of both biotite and green amphibole totalling up to 50 vol%.

Morozumi granodiorite. This unit is a minor network of irregular bodies with fine-grained texture and high biotite content (about 20 vol%). Contacts against the Morozumi Granite are either sharp or diffuse, with evidence of progressive passage to the Morozumi granite on one side and to the Morozumi diorite on the other side (Fig. 2h).

6

157   *Morozumi dykes*. The intrusive complex includes several tonalitic/granodioritic dykes

158   which, on the basis of field occurrence, have been grouped into: (i) *eastern dykes*, (ii) *western*

159   *dykes* and (iii) *crestal dykes*. The *eastern dykes* are subvertical tabular bodies conformably

160   intruding and interlayered with the foliation of the host Morozumi phyllites (Fig. 2a, d). Dykes

161   are medium-grained foliated tonalites and granodiorites with 5 to 10 vol% biotite ± muscovite.

162   At the northernmost tip of the range, the fine- to medium-grained thin peraluminous

163   leucosyenogranite dykes with muscovite ± garnet or tourmaline intruded into the

164   metasedimentary host are strongly foliated and boudinaged (Fig. 2d, g). Deformation style

165   sometimes grades to mylonitic, with asymmetric boudins indicating a west-side-up movement

166   (Fig. 2g). In other instances, fragments or streaks of Morozumi phyllites are stretched,

167   dismembered and dispersed in the host dyke (Fig. 2f). These relationships and the parallel

168   emplacement of eastern dykes and the main Morozumi granite body suggest the latter

169   intruded soon after the intrusion of the dykes that were still amid the solidification process.

170   The *western dykes* are west-dipping tabular bodies intruding the Morozumi granite at high

171   angle with the igneous foliation, and the Jupiter granite as well. When intruding the Morozumi

172   granite, dykes are fine-grained foliated tonalites with about 15 vol% biotite. Dykes intruding

173   into the Jupiter granite are medium-grained granodiorites with about 20 vol% biotite and up to

174   5 vol% muscovite. Western dikes intrude on ramps that crosscut the vertical foliation of the

175   granite host, with some ductile deformation of the granite foliation that should thus have been

176   not completely cooled down at the time of dyke emplacement. Kinematic indicators for this

177   ductile deformation indicate a top-the-east relative movement. The *crestal dykes* are tabular

178   intrusions cropping out in the summit part of the ridge: gently west-dipping tabular bodies,

179   locally cutting the intrusive foliation of the the Morozumi granite; they are fine-to medium-

180   grained leucomonzogranites to leucogranodiorites with less than 5 vol% biotite along with

181   minor muscovite. In the crestal zone of the range, the dykes crosscut the subvertical igneous

182   foliation with knife-sharp contacts (Fig. 2c) and top-to-the-east relative movement, as testified

183   by mylonitic shear at the contact (Fig. 2e), the same relative movement observed for the

184 western dykes. In summary, in the eastern side of the complex the emplacement of the granite

185 appears contemporaneous to slightly later than the dyke emplacement, while in the western

186 side and the topmost outcrops the granite foliation is crosscut by the dykes that thus were

187 emplaced when the granite was solidifying (west) or solid (crest).

188 *Jupiter granite*. This intrusive unit is named after the main spectacular outcrop in the

189 southern part of the Jupiter Amphitheatre, where a medium- to coarse-grained massive body of

190 peraluminous biotite+muscovite-monzogranite neatly crosscut the country rock (Fig. 2i). Field

191 relationships with the Morozumi granite have not been observed, while peraluminous

192 syenogranitic massive bodies of the Jupiter granite unit are intruded by tabular bodies along

193 the western flank of the intrusive complex (western tabular intrusions). Here the Jupiter

194 medium to coarse-grained granite contains igneous muscovite up to 5-10 vol%.

195 *Morozumi leucogranites/aplites*. Scattered minor bodies of fine- to medium-grained,

196 equigranular peraluminous, muscovite ± garnet or tourmaline-bearing leucosyenogranites are

197 found both within the Morozumi granite and at the contact between the granite and the host

198 schists.

199

200 **4. Analytical methodologies**

201

202 Major elements (Table 2) were determined by X-ray fluorescence (XRF-ARL 9400XP) on

203 glass beads, at Dipartimento di Scienze della Terra, Università di Pisa, with precision between

204 1% and 4% RSD for most elements, except TiO_2, MnO, CaO, Na_2O, (5–8% RSD) (Tamponi et al.,

205 2003). Trace elements (Table 2) were determined by inductively coupled plasma-mass

206 spectrometry (ICP-MS, VG PQII Plus) (Rocchi et al., 2002) at Dipartimento di Scienze della

207 Terra, Università di Pisa, after dissolution with HF-HNO_3 mixture in screw-top PFA vessels on a

208 hotplate at 120 °C. Analyses were performed by external calibration using the matrix-matching

209 geochemical reference sample BE-N. The correction procedure includes blank subtraction,

210   instrumental drift correction (Rh-Re-Bi internal standardization and repeated analysis of a

211   drift monitor), and oxide-hydroxide interference correction. Precision, evaluated by replicate

212   dissolutions and analyses of in-house and international silicate rock reference samples, is

213   generally between 2% and 5% RSD for most elements, except Cr, Ni, Pb (6–11% RSD).

214   Zirconium was determined via XRF on pressed powder pellets.

215   Sr and Nd isotopic compositions were determined using a Finnigan MAT 262V

216   multicollector mass spectrometer at Istituto di Geoscienze e Georisorse-CNR, Pisa, following

217   separation of Sr and Nd using conventional ion exchange procedures. Measured $^{87}Sr/^{86}Sr$ ratios

218   have been normalized to $^{86}Sr/^{88}Sr$ = 0.1194; $^{143}Nd/^{144}Nd$ ratios to $^{146}Nd/^{144}Nd$ = 0.7219. During

219   the course of this study, the external reproducibility for NIST-SRM987 and La Jolla Nd

220   standards were $^{87}Sr/^{86}Sr$ = 0.710250±24 and $^{143}Nd/^{144}Nd$ = 0.511858±14 (2 SD), respectively.

221   The measured Nd isotopic ratios have been adjusted to a value for La Jolla standard of

222    $^{143}Nd/^{144}Nd$ = 0.511850.

223   Geochronological data were obtained by zircon U-Pb analyses. After crushing and sieving,

224   zircons were concentrated from the 160-250 µm grain sizes using standard separation

225   techniques. About 100 zircons for each sample were cast in epoxy resin and polished to a 0.3

226   µm alumina paste finish to expose mid-section of crystals. Crystal for geochronological

227   analyses have been selected on the basis of textural observations related to inclusions,

228   occurrence/type of core and/or rim, zoning, etc carried out by Scanning Electron Microscopy-

229   Cathodoluminescence (SEM-CL) imaging by a Philips XL30 SEM at Dipartimento di Scienze

230   della Terra, Università di Pisa. U-Pb analyses by Laser Ablation-Inductively Coupled Plasma-

231   Mass Spectrometry (LA-ICP-MS) were performed at Dipartimento di Fisica e Geologia,

232   Università di Perugia (Italy) (Alagna et al., 2008) using a Thermo Electron X7 ICP-MS coupled

233   to a New Wave UP213 frequency quintupled Nd:YAG laser. U-Pb zircon analyses were

234   calibrated with standard zircon 91500 using a spot size of 25 µm and zircon GJ1 has been used

235   as quality control. The error associated with the standard reproducibility has been combined

236   quadratically with the counting statistics of each analysis.

237

5. Geochronological data

239

In order to define the temporal evolution for the emplacement of the different intrusive units, as well as to investigate differential source inheritance in different magmas, seven samples of magmatic rocks along with one sample of the metamorphic host rock have been investigated for U-Pb zircon geochronology (Table SM1).

Morozumi granite. Data from zircons with a well-preserved oscillatory magmatic zoning give a concordia age of 493.7±8.7 Ma (with decay-constant errors ignored, probability of concordance = 0.995, Fig. 3a), interpreted as the emplacement age for Morozumi granite. Zircons with ghost zoning, i.e. areas where typical igneous zoning is lacking or poorly defined, yielded younger ages and are interpreted as related to post-igneous reworking. The oldest ages clustering around 1000 Ma (Grenville-like, Fig. 4) are from three zircon cores lighter than the rim, with truncated zoning, interpreted as relict cores.

Morozumi diorite. The zircon yield was poor, comprised of tiny, elongated crystals with no well-defined oscillatory zoning and the obtained data does not allow to constrain the time of emplacement. Nevertheless, the clear hot mingling relationships with Morozumi granite (Fig. 2n) led to infer a coeval emplacement timing.

Morozumi granodiorite. Zircons with well-defined zoning have a concordia age, obtained from 5 points analysis and excluding reworked zircon areas, of 485.3±5.4 Ma (probability of concordance = 0.88, Fig. 3b). Older age clusters between 520 Ma and 650 Ma are obtained from zircons with unzoned light cores, interpreted as reworked areas. Two data points on cores give Grenvillian ages, and a single analysis yielded a Proterozoic age (Fig. 4).

Morozumi dykes. Eastern dyke. Zircon crystals are characterized by a dark core and a light rim. A few crystals have an innermost light core, and some others show oscillatory or convoluted zoned cores. Five analyses of light rims provided a Concordia Age of 496.7±6.8 Ma

263   (probability of concordance = 0.92, Fig. 3c), interpreted as the emplacement age. Three

264   additional analyses of cores give ages between ca. 550 and 1900 Ma (Fig. 4). *Western dyke.* The

265   zircon yield was modest and only 12 analyses were performed for a western dyke sample.

266   These zircons are unzoned or show convolute/ghost zoning. Six analyses (from both cores and

267   rims) range between 437±11 Ma and 573±14 Ma. The lack of any clear magmatic zoning

268   suggests post-magmatic reworking for these zircon crystals. Five additional analyses from

269   relict cores (973±23 to 1120±25 Ma) indicate the occurrence a Grenville-age component in the

270   magma source (Fig. 4).

271   *Jupiter granite.* Once data from zircons with ghost zoning were discarded, five zircon

272   crystals from sample JG1 with well-defined oscillatory zoning give a concordia age of 495.3±5.7

273   Ma (probability of concordance = 0.78, Fig. 3d), interpreted as the emplacement age. Sample

274   JG2 did yield just a few crystals, with two cores giving Grenvillian ages (Fig. 4).

275   *Morozumi phyllites.* The studied sample has been collected in the southern part of the

276   Morozumi Range, far from contacts against igneous rocks, to study a pristine sample not

277   affected by thermal effects, that are indeed not been observed in both thin sections and SEM-CL

278   zircon images. The only overgrowth observed has a $^{206}Pb/^{238}U$ age indistinguishable from that

279   of the core, within the same crystal (2299±80 vs. 2293±81 Ma, respectively). The pristine

280   characters of zircons allow to infer the youngest concordant zircon ages (571±22 and 601±22

281   Ma) as the oldest limit for the deposition of this unit, at the very end of the Neoproterozoic.

282   Younger Cambrian deposition age for the Morozumi phyllites are inferred, based on

283   unpublished dtrital zircon ages [Henjes-Kunst, 2003 #2569]. A deposition age at the boundary

284   between latest Neoproterozoic and Cambrian (c. 545 Ma) is inferred based on detrital zircon

285   ages for the Berg Group and the Priestley Formation of the Wilson terrane, as well as the Molar

286   Formation of the Bowers terrane (Adams et al., 2013).. Our data, plotted in a cumulative

287   probability plot (Fig. 4) shows a wide range of ages, with well-defined peaks slightly older than

288   600 Ma (< 20% of zircons) and around Grenville age (~ 40%); three minor peaks occur at

289   Paleoproterozoic-Archean times (total of ~ 40%). The lack of thermal imprints or

290   metamorphic overgrowths calls for a mechanism of cooling of the intruded magmas with no

291   significant conductive heating of the country rock.

292   In summary, individual intrusive units provide indistinguishable emplacement ages for the

293   main granite (493.7±8.7 Ma), the eastern dykes (496.7±6.8 Ma) and the peraluminous granite

294   (495.3±5.7 Ma). Geochronological data for the Morozumi diorite does not define an

295   emplacement age, yet field relations indicate contemporaneous emplacement with Morozumi

296   main granite (Fig. 2n). The Morozumi granodiorite provides a slightly younger nominal age of

297   485.3±5.4 Ma, although still indistinguishable at 2σ level from those of the other units, in close

298   agreement with field observations (Fig. 2h). For the Morozumi western dykes, the

299   emplacement age could not be defined geochronologically, nevertheless field relations with the

300   Morozumi granite (the dykes cut the granite igneous foliation at high angle with ductile

301   deformation of the granite) suggest once again an emplacement age almost coeval with the

302   Morozumi granite. In summary, a short time interval of no more than a few Ma around ca. 495

303   Ma is inferred for the emplacement of the whole Morozumi intrusive complex.

304   As for the relict zircon signatures, all the intrusive units (granite, granodiorite, dykes,

305   peraluminous granite) contain relict cores with Neoproterozoic and Mesoproterozoic

306   (Grenville) ages, along with rare Paleoproterozoic cores. A couple of Archean cores were found

307   only in the peraluminous Jupiter granite.

308

309   **6. Geochemical and isotopic data**

310

311   The lithological diversity of the Morozumi intrusive complex is mirrored by large

312   variabilities in the major element compositions. The Total Alkali-Silica (TAS) diagram readily

313   shows that the whole data set splits into two main subalkaline trends with different levels of

314   alkali enrichment (Fig. 5). The Morozumi diorite-granodiorite-granite samples define a roughly

315   linear trend barely reaching the granite field. At lower alkali contents, the samples from

316 Morozumi dykes define a separate roughly linear trend from the granodiorite well into the

317 granite field. Both trends have slopes that cut across the usual boundaries between magmatic

318 associations, in contrast with the typical magmatic evolution in closed systems.

319   The trace element distributions of the most mafic rocks from the two trends share common

320 features, such as a significant enrichment for the most incompatible elements, along with

321 marked negative anomalies for Nb-Ta and minor for Ti (Fig. 6). Besides those similarities, the

322 patterns also show some differences: the Morozumi diorites, despite having a silica content

323 higher than that of the most mafic Morozumi tonalite dyke, feature a higher enrichment in rare

324 earth elements (REE), most marked for heavy REE.

325   Among mafic igneous rocks from the early Paleozoic Ross Orogen of northern Victoria Land,

326 the Morozumi diorite display strong affinity to potassic rocks such as the Abbott gabbro and

327 the Vegetation lamprophyres, representing mantle-derived magmas emplaced in the late

328 orogenic to postcollisional stage (Di Vincenzo and Rocchi, 1999; Rocchi et al., 2009). Among

329 igneous rocks of comparable compositions, the Morozumi tonalite dyke has a trace element

330 distribution quite similar to that of the Confusion tonalite, a calk-alkaline unit characterizing a

331 tectonomagmatic stage earlier than the Abbott and Vegetation potassic events (Rocchi et al.,

332 2004).

333   The Sr and Nd isotopic systematics help clarifying the petrologic affinities of the Morozumi

334 igneous rocks (Fig. 7). The Morozumi diorite has Sr and Nd isotopic ratios higher and lower

335 than those of the Abbott gabbro, respectively, and definitely similar to those of the Vegetation

336 lamprophyres (Di Vincenzo and Rocchi, 1999): the Morozumi diorite has thus trace element

337 and isotopic features typical of a potassic, post-collisional magma. The Morozumi tonalite dyke

338 samples have scattered Sr isotopic compositions, making it difficult any direct comparison (see

339 further on).

340   The most felsic rocks of the two trends plot separately: a gap of 5 wt% SiO_2 separates rocks

341 with the same alkali (and K) contents. The Jupiter granite differs from all the other Morozumi

342 felsic rocks owing to its peraluminousity (Alumina Saturation Index: 1.1-1.2), and low Nd

343 isotopic ratios, coupled at odd with relatively low Sr isotopic ratios (< 0.711).

344

345 **7. Discussion - Petrogenetic issues**

346

347 The two roughly parallel compositional trends (Fig. 5) follow possible evolutionary paths

348 starting from two different parental magmas. The slopes of these trends, cutting across the

349 usual boundaries of magmatic associations (Fig. 5), coupled with Sr-Nd isotope data (Fig. 7),

350 rule out closed-system compositional evolution for both trends. The 5 wt% SiO_2 gap separating

351 felsic rocks with the same alkali (and K) contents, also lend support to the hypothesis of a

352 separate origin for the compositional groups of felsic rocks. Therefore, simple petrogenetic

353 evolutionary relationships among the various igneous units are precluded and a minimum

354 number of different magmas had to be involved in the genesis of the Morozumi complex,

355 namely: a mafic potassic dioritic melt (Morozumi diorite), a mafic tonalitic melt (Morozumi

356 mafic dykes), a felsic metaluminous granitic melt (Morozumi granite), as well as a felsic

357 peraluminous granitic melt (Jupiter granite). Additionally, a possible high-silica metaluminous

358 melt could have existed (Morozumi felsic dykes), yet field relationships indicate that a mass

359 contribution of the Morozumi phyllites to the compositional variability of the dykes has to be

360 taken into account (Fig. 2f). In the following we are going to first discuss the origin of the

361 different melts at source depth, then their interaction/evolution at shallower levels during

362 ascent/emplacement.

363

364 *7.1. What type of mantle? Origin of mafic "parental" melts:*

365

366   *Morozumi diorite.* The reconstruction of the type of mantle source activated for the

367 production of the most mafic Morozumi magmas is hampered by the absence of any rock which

could be assumed as representative of a primary mantle melt. Even the least silicic Morozumi diorite samples are indeed quite evolved, having an overall andesitic composition. Nevertheless, an origin from remelting of basaltic rocks at depth in the crust is not supported, owing to the lack of any evidence for Ross basaltic magmatism in the area. The Morozumi diorites are therefore best considered as representative of mantle melts which underwent some differentiation, potentially including open-system processes. Indeed, simple fractional crystallization is not sufficient to explain the isotopic variability of the diorite samples. Also the overall compositional trend encompassing mingled rocks (the Morozumi granodiorite show evidence for mingling-mixing relationships between the Morozumi diorite and granite melts; Fig. 2h) lend neat support to the occurrence of open-system interaction processes. To back-reconstruct the possible chemical and isotopic composition of the parental basaltic melt, a modeling of assimilation and fractional crystallization (AFC) has been run out (DePaolo, 1981). In order to derive the parameters to be used for trace element and isotopic AFC modelling, preliminary mass balance calculations have been performed: the major element composition of the finest-grained and mafic Morozumi diorite (sample 23.12.05 DS7) has been obtained starting from a common high-Al Andean basalt (Wilson, 1989) via fractionation of 9 wt% orthopyroxene, 1 wt% clinopyroxene and 25 wt% plagioclase, plus the addition of about 23 wt% of a migmatitic leucosome, with mineral and migmatite compositions after similar gabbroic-dioritic rocks from the Wilson terrane (Di Vincenzo and Rocchi, 1999). The parameters thus obtained (mass fraction crystallised = M_{FC} = 0.35; ratio of the rate of assimilation to the rate of fractional crystallisation = a = 0.66) have been used to run AFC modelling for Sr-Nd systematics, obtaining values of $^{87}Sr/^{86}Sr_{(500\ Ma)}$ = 0.706 and $\varepsilon_{Nd(500\ Ma)}$ = -1 for a possible primitive Morozumi mafic melt. These values point out that the main Morozumi original mafic melt had to have geochemical and isotopic features which are enriched compared to common primitive arc basalts. These features could either derive from (i) metasomatic enrichment in the mantle wedge, or from (ii) refilling of a fractionating-assimilating magma pond at the mantle-crust interface (R-AFC) (O'Hara, 1977), which is likely

395   to happen in a zone of underplating characterised by periodic or continuous input of fresh

396   mantle magma; this process could potentially generate enriched compositions from non-

397   enriched sub-arc mantle wedge. However, the Morozumi diorite has Sr and Nd contents that

398   are above the threshold over which a metasomatically enriched source has necessarily to be

399   invoked (Di Vincenzo and Rocchi, 1999). The zircon yield from the Morozumi diorite, although

400   quite poor, allow to establish the absence of relict cores, further supporting the full-mantle

401   origin of this magma. In conclusion, the original/parental Morozumi diorite melt had to derive

402   from a metasomatized mantle wedge characterised by an $\varepsilon_{Nd(500\ Ma)}$ not higher than -1 and a

403    $^{87}Sr/^{86}Sr_{(500\ Ma)}$ not lower than 0.706.

404   *Morozumi tonalite.* This unit does not include any rock which could be assumed as

405   representative of a primary mantle melt. Even the least silicic rock samples are quite evolved,

406   so their composition could in principle derive from several different processes. The

407   composition of tonalite is not compatible with derivation from melting of metasedimentary

408   material with protoliths such as pelites, greywackes or volcaniclastics (Fig. 8a). An alternative

409   process is the chemical evolution of a mantle melt, which however should leave some traces of

410   basic-intermediate products: the lack of products with $SiO_2 < 65$ wt% is in contrast with this

411   hypothesis. Another alternative is the crustal contamination of the Morozumi diorite melt,

412   which however conflicts with the observation that samples with the same $\varepsilon_{Nd(500\ Ma)}$ have a

413   difference of 10 wt% in the SiO_2 content. On the other hand, the Morozumi tonalites are very

414   similar to high-silica adakites for major elements composition as well as for their high La/Yb,

415   low Yb, high Sr/Y and low Y (Fig. 8b). However, the adakites interpreted as products of young

416   slab melting, as for their original definition (Defant and Drummond, 1990), usually have

417   positive ε_{Nd} (Castillo, 2012), in opposition to the low ε_{Nd} of the Morozumi tonalite melt. Such a

418   magma should therefore derive from melting of mafic material residing in the (lower?) crust.

419   Remelting of an underplate made of Morozumi potassic diorite is not likely because the

420   tonalite has much lower K content than the diorite; additionally, the observed ε_{Nd} values

421   between -5 and -6 would require melting of evolved-hybrid diorite rather than diorite itself,

422   but the observed hybridization process is limited, likely occurring en route to the emplacement

423   level, and not at the underplate level. Another potential crustal basic source is represented by

424   normal gabbros or basic amphibolites. Melting experiments (Sisson et al., 2005) indicate that

425   the Na/K/Ca relationships of the Morozumi granodiorite/tonalite are matched by melting

426   hornblende gabbro at high T (>925°C), yet these melts have SiO_2<60 wt%; using biotite- or

427   quartz-bearing hornblende gabbro as a source and/or lowering the melting temperature yields

428   products with higher SiO_2, comparable with Morozumi granodiorite/tonalite, but with

429   somewhat higher K/Ca ratios (Fig. 8a). Melting experiments of amphibolites with alkali

430   basaltic and island arc tholeiitic composition (Rushmer, 1991) yield melts with lower SiO_2 and

431   higher Ca/Na ratios with respect to the Morozumi tonalite (Fig. 8a); on the other hand,

432   "synthetic amphibolites" (a mix of hornblende, albite and quartz) at high T=975 °C give melts

433   with a composition compatible with the Morozumi tonalite (Rushmer, 1991). Also the

434   occurrence of even a few old zircons with variable Proterozoic ages helps ruling out simple

435   young slab or underplate melting, rather supporting addition of some crustal material to the

436   mantle wedge. The process responsible of such an addition could be ascribed to the category of

437   subduction erosion that can also explain strong REE fractionation coupled with high Sr content

438   without invoking subduction of young slab at garnet depth (Kay et al., 2005). Large-scale

439   subduction erosion or even larger-scale subduction of small continental block(s) can bring into

440   the mantle wedge crustal materials, which then exhumes due to slab roll-back, becomes

441   incorporated into the overriding plate (Brun and Faccenna, 2008) and can contribute to melt

442   generation.

443

444   *7.2. What type of crust? Origin of felsic melts*

445

446   The four types of felsic intrusive units of the Morozumi complex have very different sizes:

447   the Morozumi granite is by far the most voluminous, constituting most of the mass of the

448   intrusive complex; the Jupiter peraluminous granites are found in two main large outcrops; the

449   Morozumi leucogranites represent very small, vein- or pod-like bodies; the Morozumi dykes

450   with felsic composition are leucogranitic portions of tonalite-granodiorite dykes. The chemical

451   and isotopic compositions of these four felsic rock types point out that they also have distinct

452   origins.

453   The Jupiter granite and the vein-like Morozumi leucogranites have compositions typical of

454   minimum melts from metasedimentary protoliths such as greywacke or pelite rocks (Fig. 8a).

455   These minor units have Sr-Nd compositions displaced from the main trend towards lower Sr

456   isotopic ratios (Fig. 7), as observed elsewhere for melting occurring in disequilibrium

457   conditions (Farina et al., 2014; Farina and Stevens, 2011; Harris and Ayres, 1998). Relict

458   zircons show an age spectrum including scattered evidence for recycling of early Proterozoic

459   and Archean material. In synthesis, the source that can be inferred for the Jupiter granite is a

460   late Proterozoic metasedimentary upper crust.

461   On the other hand, the main Morozumi granite has a composition that is too Ca-rich to be

462   derived from melting of common pelite-metagreywacke-volcaniclastic sources (Fig. 8a).

463   Morozumi granites have Sr-Nd isotopic compositions that plot on the general trend linking

464   mantle products and crustal magmatic rocks deriving from melting of different crustal levels,

465   from deep granulite to upper crust metasediments (Di Vincenzo and Rocchi, 1999). Low $\varepsilon_{Nd(500}$

466    $_{Ma)}$ and moderately high $^{87}Sr/^{86}Sr_{(500\ Ma)}$ lead to prefer a granulite source. The cargo of relict

467   zircons of the Morozumi granite is restricted to Grenvillian and mid-Neoproterozoic ages.

468   Overall, the origin that can be envisaged for the main Morozumi granite is from melting of a

469   Grenville-age deep crustal granulite, isotopically similar to the enderbites and metaenderbites

470   from northern Victoria Land, which have $^{87}Sr/^{86}Sr_{(500\ Ma)}$=0.710 to 0.714 and $\varepsilon_{Nd(500\ Ma)}$= -7.8 to -

471 8.4, in turn geochemically similar to the Grenville-age Antarctic charnockites (Talarico et al.,

472 1995).

473   The leucogranitic portions of the Morozumi dykes have Na-Ca-K relationships (Fig. 9) and

474 Sr-Nd isotopic ratios (Fig. 7) potentially relating them to a source similar to that of the

475 Morozumi granite. However, their higher silica content (Fig. 8a) and their field and

476 geochemical relationships with host rocks suggest a different scenario (see further on).

477

478 *7.3. Shallow processes: Origin of the diorite-granite trend*

479

480   The rocks forming this trend (diorite, granodiorite, granite) display field evidence attesting

481 for mingling-mixing relationships among them: dioritic melt did form pillows within the

482 granite melt (Fig. 2n), and diffuse diorite-granite contacts are observed, with a granodiorite

483 facies in between (Fig. 2h). Effective mixing was likely limited, as suggested by the minor

484 volume of the granodiorite facies. Additionally, the granodiorite sometimes show angular

485 blocks in sharp contact towards the host main granite, suggesting that the mingling process

486 was limited, and rapidly evolved to more rigid behaviour. Chemical data (Fig. 5) and Sr-Nd

487 isotopic systematics (Figs. 7 and 9) support field observations, with the granodiorite values

488 fitting a simple mixing trend between the diorite and granite compositions.

489

490 *7.4. Shallow processes: Origin of the tonalite-leucogranite trend*

491

492   The Morozumi dykes metaluminous tonalites grade into evolved products in which white

493 mica becomes a main mineral phase. This suggests a possible interaction with a peraluminous

494 material. Potential candidates are both the Jupiter granite and the very minor

495 aplite/leucogranites or the metasedimentary country rock. However, field evidence of

496 stretched portions and streaks of mica-rich material incorporated from the host schist (Fig. 2f)

19

497   into the subvertical eastern dykes suggests that the tonalite melt did engulf and stretch

498   variable amounts of schist, leading to progressively silica-richer, more peraluminous

499   compositions. Also in this case, field evidence is supported by Sr isotopic data (Fig. 9)

500   indicating mixing relationships between the most primitive and the most evolved dykes.

501   However, the lack of any evidence for thermal metamorphism in the host schist suggests that

502   the interaction process was quick, with very limited heat transfer. Therefore, the term mixing

503   is here used to describe the chemical result of the process, yet from the petrographic point of

504   view the schist is just incorporated, stretched, dismembered and dispersed in the melt to the

505   point that distiguishing the origin of single crystals is actually a hard, if possible, task.

506

507   **8. Summary and implications**

508

509   Field evidence, coupled with geochronological and petrographic-chemical-isotopic data

510   outline a scenario of coeval emplacement of distinct melts issuing from different sources in the

511   mantle and from different crustal levels as well (Fig. 10). These melts were interacting

512   between them and/or with country rock during emplacement in a swiftly changing tectonic

513   regime.

514

515   *8.1. Magma origin and emplacement*

516

517   Distinct magma sources were activated at almost the same time in the metasomatized

518   mantle, in the upper crust, in the lower crust and in a domain where mantle and crust were

519   mixed up by subduction erosion. The first magma emplaced in the Morozumi complex was a

520   tonalite melt, intruded as subvertical dykes, parallel to the host schist foliation (Fig. 2a, d). The

521   almost simultaneous emplacement of the main Morozumi granitic melt did generate a local

522   compressional (flattening) regime with subhorizontal σ_1 leading to boudinage (Fig. 2g) of the

523   vertically emplacing tonalite magma (Fig. 2a, d) which incorporated pieces of the host schists

524   which were further stretched and dismembered into the crystallizing melt (Fig. 2f, g). The main

525   intrusive body of the Morozumi granite was emplaced taking the shape of a subvertical large

526   tabular body (Fig. 2a) with vertical magmatic foliation and lineation (Fig. 2b, l), in a transient

527   stress regime ruled by the emplacement of main granitic melt. After that, the regional stress

528   became dominant again, and further tonalite melt was thus intruded crosscutting the vertical

529   foliation in a top-to-the-east thrusting regime evolving from ductile (melt present, Fig. 2l, o) to

530   mylonitic (Fig. 2c, e). The emplacement regime of the peraluminous Jupiter granite can be

531   inferred only from its intrusive relationships with the host schist, that indicate a brittle regime

532   with shallowly dipping contacts (Fig. 2i), suggesting an overall tectonic regime finally coming

533   to a rest.

534   Thus, four different melts were produced from the Morozumi lithospheric section in a short

535   time span around 495 Ma (Fig. 10): (1) peraluminous granitic melts from the upper crust, (2)

536   significant volumes of magma produced from recycling of Grenville-age, granulitic lower crust,

537   (3) small volumes of tonalite melt deriving from subduction erosion-enriched mantle wedge,

538   and (4) minor mafic melt from a metasomatized mantle. The contemporaneous activation of

539   these four different sources is a remarkable example of the complexity of magma sources

540   involved in a magmatic arc. Overall, it suggests that physical conditions for partial melting

541   were attained contemporaneously in domains usually found at very different depths, and that

542   produced melts found common pathways to emplace in the same site in the arc. In a

543   subduction arc setting, such a scenario can occur when a relevant process of subduction

544   erosion, possibly combined with underthrusting, bring into the sub-arc mantle large slices of

545   upper and lower continental crust, and in the mantle wedge minor amounts of crustal material.

546

547   *8.2. Geodynamic implications*

548

549   Such a scenario fits well into the space-time geological setting of the Morozumi Range

550   intrusive complex, which is located in the area facing the classical boundary between Wilson

551   and Bowers terranes and was built up by the latest pulses of the Wilson magmatic arc, a few

552   Ma after the docking of the Bowers arc-backarc system against the Wilson arc, which did occur

553   a few km to the NE (Rocchi et al., 2011). The deeply underthrusted slices of continental crust

554   and mafic material of the arc-backarc system reached ultra-high-pressure depths (Palmeri et

555   al., 2011) and were soon exhumed, making it available in the mantle wedge and the overriding

556   plate different sources such as metasomatized mantle, old lower crust and upper crust as well.

557   Magma thus generated, rose and emplaced in the Morozumi Range in a NE-SW convergent

558   tectonic regime, evolving to top-to-the NE midcrustal shearing (Rossetti et al., 2011) linked to

559   the final docking from the NE of the Admiralty ribbon (Rocchi et al., 2011), also called

560   Admiralty Block (Rossetti et al., 2011).

561   In a larger, orogen-scale view, this scenario leads to infer that the Antarctic margin of

562   Gondwana in Victoria Land during Cambrian-Ordovician times was behaving in a differential

563   way at different -current- latitudes. In the central Transantarctic Mountains, simple Sr-Nd

564   isotope trends across the chain (Borg et al., 1990) indicate near-orthogonal subduction.

565   Towards the north, in central Vicoria Land and southernmost northern Victoria Land, the

566   margin behaved in a more complex way, with along-strike shifting of forearc slivers (Rocchi et

567   al., 1998). In northernmost northern Victoria Land, multiple continental and oceanic arcs were

568   active, and convergence was not a straightforward process, rather accretion did alternate with

569   detachment of continental material-laden forearc-backarc from the main margin (Rocchi et al.,

570   2011). In the southernmost sectors, a single subduction zone is invoked (Goodge et al., 2012),

571   and a tectonic lock-up finally occurred at around 490 Ma, with production of postcollisional

572   lamprophyres and granites emplaced in a brittle regime (Rocchi et al., 2009). Differently, the

573   northern sector was characterized by a more complex geodynamic evolution, with alternating

574   periods of single or double SW-verging active subduction zones, and contractional-

575   accretionary stages alternated with extensional periods of the supra-subduction forearc

576 (Rocchi et al., 2011). In this framework, the classification of granites in syn- or post-tectonic

577 becomes increasingly meaningless towards the north, where deformation occurred at several

578 stages, until during the emplacement of very late intrusions, and even after that (Di Vincenzo et

579 al., 2007), in absence of coeval magmatic activity.

580

586

587 **Tables**

588

589 Table 1.   Summary of field, petrographic and geochronological features of the lithologic

590   units of the Morozumi Range intrusive complex..

591 Table 2.   Major elements, trace elements and Sr-Nd isotopic data.

592 Table SM1.   U-Pb LA-ICP-MS zircon data.

593

594 **Figure Captions**

595

596 Fig. 1.   (a) Location map of the Transantarctic Mountains and Victoria Land in the frame of

597   the early Paleozoic Ross-Delamerian orogen in Antarctica-Australia-Tasmania before

598   the breakup of Gondwana (Foster et al., 2005; Glen, 2005). (b) Satellite view of

599   Victoria Land, based on http://rapidfire.sci.gsfc.nasa.gov. For comparison between

600   the representation of Victoria Land reported here (Rocchi et al., 2011) and that

601 reported in papers using the classical partition of northern Victoria Land into three
602 terranes: (i) the Wilson terrane is here represented by the Wilson continental arc, (ii)
603 the Bowers terrane is represented by the Bowers arc-backarc plus the southernmost
604 part of the Tiger arc, and (iii) the Robertson Bay terrane is represented by the
605 Admiralty crustal ribbon plus the northernmost part of the Tiger arc. IG:
606 "postcollisional" granites and felsic dykes; VL: "postcollisional" lamprophyric dykes
607 (Rocchi et al., 2009). (c) Magnification of the Morozumi Range, with location of field
608 photographs reported in Figure 2.

609 Fig. 2. Field photographs of the Morozumi Range intrusive complex. (a) Panoramic view
610 from NE of the northern Morozumi Range, vertical relief 1300 m, horizontal view ca.
611 10 km. Dark rocks: Morozumi phyllites; light rocks: Morozumi granite. (b) Morozumi
612 granite, width of viewfield 40 cm. (c) Morozumi crestal dyke intruding Morozumi
613 granite with a top-to-the-east shear band at the lower contact. (d) Morozumi Range,
614 view from NW: Morozumi granite on the right (west), Morozumi phyllites to the left
615 (east) intruded by Morozumi eastern dykes. (e) Detail of (c): top-to-the-east shear
616 band at the contact between Morozumi crestal dyke (above) intruding Morozumi
617 granite (below). (f) Streaks of stretched Morozumi phyllites into Morozumi eastern
618 dyke; person for scale. (g) Stretched portions of eastern dykes (light colour), with
619 asymmetric boudinage structures, intruded into Morozumi phyllites (dark); hammer
620 for scale. (h) Detail of (m): diffuse contact between Morozumi diorite, granodiorite
621 and granite; hammers for scale. (i) Jupiter granite, light-coloured, intruding Morozumi
622 phyllites with subhorizontal contact at Jupiter Amphitheatre; vertical relief 300 m. (l)
623 Western dyke, below, intruding Morozumi granite; person for scale. (m) Dykes and
624 stocks of Morozumi diorite intruding Morozumi granite; persons for scale. (n) Detail
625 of (m): pillows of Morozumi diorite into a felsic facies of Morozumi granite at the
626 diorite-granite contact; hammer for scale. (o) Detail of (l): western dyke (below),
627 intruding vertically foliated Morozumi granite and aplite as well; hammer for scale.

628   Fig. 3. $^{206}Pb/^{238}U$ vs $^{207}Pb/^{235}U$ concordia plots for concordant ages with a 2σ error. Plots and

629   concordia ages obtained by Isoplot software (Ludwig, 2012). Representative SEM-CL

630   images are reported.

631   Fig. 4.   Cumulative probability distribution (Ludwig, 2012) of $^{206}Pb/^{238}U$ ages for the

632   Morozumi intrusive units and host rocks. Representative SEM-CL images are

633   reported.

634   Fig. 5.   Total Alkali-Silica (TAS) diagram of the Morozumi intrusive units. Also reported for

635   comparison: (i) intrusive rocks emplaced at 490-500 Ma in the Wilson arc: (i) Abbott

636   gabbro, Confusion tonalites, Abbott granites, Vegetation leucogranites (Di Vincenzo

637   and Rocchi, 1999; Rocchi et al., 2004), Vegetation lamprophyres and Irizar granites-

638   dykes (Rocchi et al., 2009), and (ii) intrusive rocks emplaced earlier in the Tiger

639   oceanic arc, i.e. Tiger gabbro (Bracciali et al., 2009).

640   Fig. 6.   N-MORB-normalized plots (Sun and McDonough, 1989) of incompatible elements. (a)

641   Morozumi diorite samples, compared to the Abbott gabbro (Di Vincenzo and Rocchi,

642   1999), the Vegetation lamprophyres from central Victoria Land (Rocchi et al., 2009)

643   and the Tiger gabbro from the Tiger magmatic arc (Fig. 1) (Bracciali et al., 2009). (b)

644   Morozumi tonalite dyke, compared to the Confusion tonalite (Di Vincenzo and Rocchi,

645   1999; Rocchi et al., 2004) and the Tiger gabbro from the Tiger magmatic arc (Fig. 1)

646   (Bracciali et al., 2009).

647   Fig. 7. $\varepsilon_{Nd\,(500\,Ma)}$ vs $^{87}Sr/^{86}Sr_{(500\,Ma)}$ plot of the Morozumi mafic-intermediate intrusive rocks.

648   Also reported for comparison: (i) intrusive complexes emplaced at around 490-500

649   Ma in the Wilson arc: (i) the Abbott gabbro and its hybridization trend with melts

650   from the deep crust, the Confusion tonalites, Vegetation leucogranites and their

651   hybridization trend with melts from mesedimentary upper crust (Di Vincenzo and

652   Rocchi, 1999; Rocchi et al., 2004), (ii) the Irizar granites and dykes (Rocchi et al.,

653   2009), and (iii) intrusive rocks emplaced earlier in the Tiger oceanic arc, i.e. Tiger

654   gabbro (Bracciali et al., 2009).

655 Fig. 8. (a) Ternary diagrams showing Na-K-Ca relationships for the rocks of the Morozumi

656 intrusive complex compared to pelite-, greywacke- and metavolcanoclastics-derived

657 fluid-absent experimental melts (Montel and Vielzeuf, 1997; Patiño Douce and Beard,

658 1996; Patiño Douce and Johnston, 1991; Sisson et al., 2005; Skjerlie and Johnston,

659 1996; Stevens et al., 1997; Vielzeuf and Holloway, 1988) and to adakite and TTG fields

660 and evolutionary trends (Defant and Drummond, 1993). (b) Classical Sr/Y vs. Sr plot

661 comparing the Morozumi mafic-intermediate intrusive rocks with the adakite and

662 andesite-dacite-rhyolite (ADR) fields (Defant and Drummond, 1993)

663 Fig. 9. $^{87}Sr/^{86}Sr$ vs. 1000/Sr plot, showing mixing trends as linear paths.

664 Fig. 10. Idealized sketch of the reconstructed scenario from the emplacement level down to

665 source depth.

666

667 **References**

668 Adams, C.J., Bradshaw, J.D., Ireland, T.R., 2013. Provenance connections between late
669 Neoproterozoic and early Palaeozoic sedimentary basins of the Ross Sea region,
670 Antarctica, south-east Australia and southern Zealandia. Antarctic Science 26, 173-
671 182.
672 Alagna, K.E., Petrelli, M., Perugini, D., Poli, G., 2008. Micro-Analytical Zircon and
673 Monazite U-Pb Isotope Dating by Laser Ablation-Inductively Coupled Plasma-
674 Quadrupole Mass Spectrometry. Geostandards and Geoanalytical Research 32, 103-
675 120.
676 Allibone, A., Wysoczanski, R., 2002. Initiation of magmatism during the Cambro-
677 Ordovician Ross orogeny in southern Victoria Land, Antarctica. Geological Society of
678 America Bulletin 114, 1007-1018.
679 Boger, S.D., Miller, J.M., 2004. Terminal suturing of Gondwana and the onset of the Ross-
680 Delamerian Orogeny: the cause and effect of an Early Cambrian reconfiguration of
681 plate motions. Earth and Planetary Science Letters 219, 35-48.
682 Bomparola, R.M., Ghezzo, C., Belousova, E., Griffin, W.L., O'Reilly, S.Y., 2007. Resetting
683 of the U-Pb zircon system in Cambro-Ordovician intrusives of the Deep Freeze Range,
684 northern Victoria Land, Antarctica. Journal of Petrology 48, 327-364.
685 Borg, S.G., DePaolo, D.J., Smith, B.M., 1990. Isotopic structure and tectonics of the Central
686 Tansantarctic Mountains. Journal of Geophysical Research 95, 6647-6667.
687 Bracciali, L., Di Vincenzo, G., Rocchi, S., Ghezzo, C., 2009. The Tiger Gabbro from
688 northern Victoria Land, Antarctica: the roots of an island arc within the early
689 Palaeozoic margin of Gondwana. Journal of the Geological Society, London 166, 711-
690 724.
691 Bradshaw, J.D., Weaver, S.D., Laird, M.G., 1985. Suspect Terranes and Cambrian Tectonics
692 in Northern Victoria Land, Antarctica, in: Howell, D.G. (Ed.), Tectonostratigraphic

Terranes of the Circum-Pacific Region, Circum-Pacific Conference for Energy and Mineral Resources, Earth Science Series, pp. 467-479.

Brown, M., 2013. Granite: From genesis to emplacement. Geological Society of America Bulletin 125, 1079-1113.

Brun, J.-P., Faccenna, C., 2008. Exhumation of high-pressure rocks driven by slab rollback. Earth and Planetary Science Letters 272, 1-7.

Castillo, P.R., 2012. Adakite petrogenesis. Lithos 134–135, 304-316.

Cawood, P.A., 2005. Terra Australis Orogen: Rodinia breakup and development of the Pacific and Iapetus margins of Gondwana during the Neoproterozoic and Paleozoic. Earth Science Reviews 69, 249-279.

Crispini, L., Di Vincenzo, G., Palmeri, R., 2007. Petrology and ^{40}Ar–^{39}Ar dating of shear zones in the Lanterman Range (northern Victoria Land, Antarctica): implications for metamorphic and temporal evolution at terrane boundaries. Mineralogy and Petrology 89, 217-249.

Davidson, J.P., Hora, J.M., Garrison, J.M., Dungan, M.A., 2005. Crustal forensics in arc magmas. Journal of Volcanology and Geothermal Research 140, 157-170.

Defant, M.J., Drummond, M.S., 1990. Derivation of some modern arc magmas by melting of young subducted lithosphere. Nature 347, 662-665.

Defant, M.J., Drummond, M.S., 1993. Mount St. Helens: potential example of the partial melting of the subducted lithosphere in a volcanic arc. Geology 21, 541–550. Geology 21, 547-550.

DePaolo, D.J., 1981. Trace element and isotopic effects of combined wallrock assimilation and fractional crystallisation. Earth and Planetary Science Letters 53, 189-202.

Di Vincenzo, G., Carosi, R., Palmeri, R., Tiepolo, M., 2007. A comparative U–Th–Pb (zircon–monazite) and ^{40}Ar–^{39}Ar (muscovite–biotite) study of shear zones in northern Victoria Land (Antarctica): implications for geochronology and localized reworking of the Ross Orogen. Journal of Metamorphic Geology 25, 605-630.

Di Vincenzo, G., Grande, a., Rossetti, F., 2014. **Paleozoic siliciclastic rocks from northern Victoria Land (Antarctica): Provenance, timing of deformation, and implications for the Antarctica-Australia connection**. Geological Society of America Bulletin 126, 1416-1438.

Di Vincenzo, G., Rocchi, S., 1999. Origin and interaction of mafic and felsic magmas in an evolving late orogenic setting: the early Paleozoic Terra Nova Intrusive Complex, Antarctica. Contributions to Mineralogy and Petrology 137, 15-35.

Encarnación, J., Grunow, A., 1996. Changing magmatic and tectonic style along the paleo-Pacific margin of Gondwana and the onset of early Paleozoic magmatism in Antarctica. Tectonics 15, 1325-1341.

Farina, F., Dini, A., Rocchi, S., Stevens, G., 2014. Extreme mineral-scale Sr isotope heterogeneity in granites by disequilibrium melting of the crust. Earth and Planetary Science Letters 399, 103-115.

Farina, F., Stevens, G., 2011. Source controlled 87Sr/86Sr isotope variability in granitic magmas: The inevitable consequence of mineral-scale isotopic disequilibrium in the protolith. Lithos 122, 189-200.

Federico, L., Capponi, G., Crispini, L., 2006. The Ross orogeny of the transantarctic mountains: a northern Victoria Land perspective. International Journal of Earth Sciences 95, 759-770.

Ferraccioli, F., Armadillo, E., Zunino, A., Bozzo, E., Rocchi, S., Armienti, P., 2009. Magmatic and tectonic patterns over the Northern Victoria Land sector of the Transantarctic Mountains from new aeromagnetic imaging. Tectonophysics 478, 43-61.

Ferraccioli, F., Bozzo, E., Capponi, G., 2002. Aeromagnetic and gravity anomaly constraints for an early Paleozoic subduction system of Victoria Land, Antarctica. Geophysical Research Letters 29, 10.1029/20012001GLO20014138.

Finn, C., Moore, D., Damaske, D., Mackey, T., 1999. Aeromagnetic legacy of early subduction along the Pacific margin of Gondwana. Geology 27, 1087-1090.

Flöttmann, T., Gibson, G.M., Kleinschmidt, G., 1993. Structural continuity of the Ross and Delamerian orogens of Antarctica and Australia along the margin of the paleo-Pacific. Geology 21, 319-322.

Foden, J., Elburg, M.A., Dougherty-Page, J., Burtt, A., 2006. The timing and duration of the Delamerian Orogeny: correlation with the Ross Orogen and implications for Gondwana assembly. Journal of Geology 114, 189-210.

Foster, D.A., Grey, D.R., Spaggiari, C., 2005. Timing of subduction and exhumation along the Cambrian East Gondwana margin, and the formation of Paleozoic backarc basins. Geological Society of America Bulletin 117, 105-116.

GANOVEX TEAM, 1987. Geological Map of North Victoria Land, Antarctica, 1:500,000 - Explanatory notes -. Geologisches Jahrbuch B66, 7-79.

Gemelli, M., Rocchi, S., Di Vincenzo, G., Petrelli, M., 2009. Accretion of juvenile crust at the Early Palaeozoic Antarctic margin of Gondwana: geochemical and geochronological evidence from granulite xenoliths. Terra Nova 21, 151-191.

Giacomini, F., Tiepolo, M., Dallai, L., Ghezzo, C., 2007. On the onset and evolution of the Ross-orogeny magmatism in North Victoria Land - Antarctica. Chemical Geology 240, 103-128.

Gibson, G.M., Ireland, T.R., 1996. Extension of Delamerian (Ross) orogen into western New Zealand: Evidence from zircon ages and implications for crustal growth along the Pacific margin of Gondwana. Geology 24, 1087-1090.

Gibson, G.M., Morse, M.P., Ireland, T.R., Nayak, G.K., 2011. Arc-continent collision and orogenesis in western Tasmanides: Insights from reactivated basement structures and formation of an ocean-continent transform boundary off western Tasmania. Gondwana Research 19, 608-627.

Gibson, G.M., Wright, T.O., 1985. Importance of thrust faulting in the tectonic development of northern Victoria Land, Antarctica. Nature 315, 480-483.

Glen, R.A., 2005. The Tasmanides of eastern Australia, in: Vaughan, A.P.M., Leat, P.M., Pankhurst, R.J. (Eds.), Terrane processes at the margins of Gondwana. Geological Society Special Publications, 246, London, pp. 23-96.

Glen, R.A., 2013. Refining accretionary orogen models for the Tasmanides of eastern Australia. Australian Journal of Earth Sciences 60, 315-370.

Glen, R.A., Meffre, S., Scott, R.J., 2007. Benambran Orogeny in the Eastern Lachlan Orogen, Australia. Australian Journal of Earth Sciences: An International Geoscience Journal of the Geological Society of Australia 54, 385 - 415.

Goodge, J.W., 2002. From Rodinia to Gondwana: supercontinent evolution in the Transantarctic Mountains, in: Gamble, J.A., Skinner, D.N.B., Henrys, S. (Eds.), Proceedings of the 8th International Symposium on Antarctic Earth Sciences, Royal Society of New Zealand Bulletin, pp. 61-74.

Goodge, J.W., Fanning, C.M., Norman, M.D., Bennett, V.C., 2012. Temporal, Isotopic and Spatial Relations of Early Paleozoic Gondwana-Margin Arc Magmatism, Central Transantarctic Mountains, Antarctica. Journal of Petrology 53, 2027-2065.

Goodge, J.W., Williams, I.S., Myrow, P., 2004. Provenance of Neoproterozoic and lower Paleozoic siliciclastic rocks of the central Ross orogen, Antarctica: Detrital record of rift-, passive-, and active-margin sedimentation. Geological Society of America Bulletin 116, 1253-1279.

Hacker, B.R., Kelemen, P.B., Behn, M.D., 2011. Differentiation of the continental crust by relamination. Earth and Planetary Science Letters 307, 501-516.

Harris, N., Ayres, M., 1998. The implications of Sr-isotope disequilibrium for rates of prograde metamorphism and melt extraction in anatectic terrains, in: Treloar, P.J., O'Brien, P.J. (Eds.), What drives metamorphism and metamorphic reactions? Geological Society, London, Special Publication, pp. 171-182.

Kay, S.M., Godoy, E., Kurtz, A., 2005. Episodic arc migration, crustal thickening, subduction erosion, and magmatism in the south-central Andes. Geological Society of America Bulletin 117, 67-88.

Kleinschmidt, G., Tessensohn, F., 1987. Early Paleozoic westward directed subduction at the Pacific continental margin of Antarctica, Sixth Gondwana Symposium. American Geophysical Union, Geophysical Monograph, 40, pp. 89-105.

Ludwig, K.R., 2012. Isoplot/Ex 3.75, 3.00 ed. Berkeley Geochronology Center, Special Publication No. 4.

Montel, J.-M., Vielzeuf, D., 1997. Partial melting of metagreywackes, Part II. Compositions of minerals and melts. Contributions to Mineralogy and Petrology 128, 176-196.

O'Hara, M.J., 1977. Geochemical evolution during fractional crystallisation of a periodically refilled magma chamber. Nature 266, 503-507.

Palmeri, R., Talarico, F.M., Ricci, C.A., 2011. Ultrahigh-pressure metamorphism at the Lanterman Range (northern Victoria Land, Antarctica). Geological Journal 46, 126-136.

Patiño Douce, A.E., Beard, J.S., 1996. Effect of P, f(O2) and Mg/Fe ratio on dehydration melting of model metagreywackes. Journal of Petrology 37, 999-1024.

Patiño Douce, A.E., Johnston, A.D., 1991. Phase equilibria and melt productivity in the pelitic system: implications for the origin of peraluminous granitoids and aluminous granulites. Contributions to Mineralogy and Petrology 107, 202-218.

Pearce, J.A., Peate, D.W., 1995. Tectonic implications of the composition of volcanic arc magmas. Annual Revue of Earth and Planetary Sciences 23, 251-285.

Rocchi, S., Armienti, P., D'Orazio, M., Tonarini, S., Wijbrans, J., Di Vincenzo, G., 2002. Cenozoic magmatism in the western Ross Embayment: role of mantle plume vs. plate dynamics in the development of the West Antarctic Rift System. Journal of Geophysical Research 107, 2195.

Rocchi, S., Bracciali, L., Di Vincenzo, G., Gemelli, M., Ghezzo, C., 2011. Arc accretion to the early Paleozoic Antarctic margin of Gondwana in Victoria Land. Gondwana Research 19, 594-607.

Rocchi, S., Capponi, G., Crispini, L., Di Vincenzo, G., Ghezzo, C., Meccheri, M., Palmeri, R., 2003. Mafic rocks at the Wilson-Bowers terrane transition and within the Bowers terrane: implications for a geodynamic model of the Ross Orogeny. Terra Antartica Reports 9, 145-148.

Rocchi, S., Di Vincenzo, G., Ghezzo, C., 2004. The Terra Nova Intrusive Complex (Victoria Land, Antarctica), with 1:50,000 Geopetrographic Map. Terra Antartica Reports 10, 51.

Rocchi, S., Di Vincenzo, G., Ghezzo, C., Nardini, I., 2009. Granite-lamprophyre connection in the latest stages of the Early Paleozoic Ross Orogeny (Victoria Land, Antarctica). Geological Society of America Bulletin 121, 801-819.

Rocchi, S., Tonarini, S., Armienti, P., Innocenti, F., Manetti, P., 1998. Geochemical and isotopic structure of the early Palaeozoic active margin of Gondwana in northern Victoria Land, Antarctica. Tectonophysics 284, 261-281.

Roland, N.W., Läufer, A., Rossetti, F., 2004. Revision of the terrane model of northern Victoria Land. Terra Antartica 11, 55-65.

843 Rossetti, F., Storti, F., Busetti, M., Di Vincenzo, G., Lisker, F., Rocchi, S., Salvini, F.,
844   2006a. Eocene initiation of Ross Sea dextral faulting and implications for East
845   Antarctic neotectonics. Journal of the Geological Society, London 163, 119-126.
846 Rossetti, F., Tecce, F., Aldega, L., Brilli, M., Faccenna, C., 2006b. Deformation and fluid
847   flow during orogeny at the palaeo- active margin of Gondwana: the Early Palaeozoic
848   Robertson accretionary complex (north Victoria Land, Antarctica). Journal of
849   Metamorphic Geology 24, 33-53.
850 Rossetti, F., Vignaroli, G., Di Vincenzo, G., Gerdes, A., Ghezzo, C., Theye, T., Balsamo, F.,
851   2011. Long-lived orogenic construction along the paleo-Pacific margin of Gondwana
852   (Deep Freeze Range, North Victoria Land, Antarctica). Tectonics 30, TC4008.
853 Rushmer, T., 1991. Partial melting of two amphibolites: contrasting experimental results
854   under fluid-absent conditions. Contributions to Mineralogy and Petrology 107, 41-59.
855 Sisson, T.W., Ratajeski, K., Hankins, W.B., Glazner, A.F., 2005. Voluminous granitic
856   magmas from common basaltic sources. Contributions to Mineralogy and Petrology
857   148, 635–661.
858 Skjerlie, K.P., Johnston, A.D., 1996. Vapour-absent melting from 10 to 20 kbar of crustal
859   rocks that contain multiple hydrous phases: implications for anatexis in the deep to
860   very deep continental crust and active continental margins. Journal of Petrology 37,
861   661-691.
862 Stevens, G., Clemens, J.D., Droop, G.T.R., 1997. Melt production during granulite-facies
863   anatexis: experimental data from "primitive" metasedimentary protoliths.
864   Contributions to Mineralogy and Petrology 128, 352-370.
865 Stump, E., 1995. The Ross Orogen of the Transantarctic Mountains. Cambridge University
866   Press, Cambridge.
867 Stump, E., Gootee, B., Talarico, F., 2006. Tectonic model for development of the Byrd
868   Glacier Discontinuity and surrounding regions of the Transantarctic Mountains during
869   the Neoproterozoic - Early Paleozoic, in: Fütterer, D.K., Damaske, D., Kleinschmidt,
870   G., Miller, H., Tessensohn, F. (Eds.), Antarctica – Contributions to Global Earth
871   Sciences, Proceedings of the IX International Symposium of Antarctic Earth Sciences,
872   Potsdam, 2003. Springer-Verlag, Berlin Heidelberg New York, pp. 181-190.
873 Stump, E., Laird, M.G., Bradshaw, J.D., Holloway, J.R., Borg, S.G., Lapham, K.E., 1983.
874   Bowers graben and associated tectonic features cross northern Victoria Land,
875   Antarctica. Nature 304, 334-336.
876 Stump, E., White, A.J.R., Borg, S.G., 1986. Reconstruction of Australia and Antarctica:
877   evidence from granites and recent mapping. Earth and Planetary Science Letters 79,
878   348-360.
879 Sun, S.S., McDonough, W.F., 1989. Chemical and isotopic systematics of oceanic basalts:
880   implications for mantle composition and processes, in: Saunders, A.D., Norry, M.J.
881   (Eds.), Magmatism in the Ocean Basins. Geological Society of London Special
882   Publication, pp. 313-345.
883 Talarico, F., Borsi, L., Lombardo, B., 1995. Relict granulites of the Ross Orogen of northern
884   Victoria Land (Antarctica). II - Geochemistry and paleo-tectonic implications.
885   Precambrian Research 75, 157-174.
886 Tamponi, M., Bertoli, F., Innocenti, F., Leoni, L., 2003. X-ray fluorescence analysis of
887   major elements in silicate rocks using fused glass discs. Atti della Società Toscana di
888   Scienze Naturali, Memorie Serie A 107, 73-80.
889 Tessensohn, F., Henjes-Kunst, F., 2005. Northern Victoria Land terranes, Antarctica: far
890   travelled or local products?, in: Vaughan, A.P.M., Leat, P., Pankhurst, R.J. (Eds.),
891   Terrane processe at the margin of Gondwana. Geological Society, London, Special
892   Publications, 246, pp. 275-291.

893   Turner, S., Haines, P., Foster, D., Powell, R., Sandiford, M., Offler, R., 2009. Did the
894   Delamerian Orogeny Start in the Neoproterozoic? The Journal of Geology 117, 575-
895   583.
896   Vielzeuf, D., Holloway, J.R., 1988. Experimental determination of the fluid-absent melting
897   relations in the pelitic system. Consequences for crustal differentiation. Contributions
898   to Mineralogy and Petrology 98, 257-276.
899   von Huene, R., Ranero, C.R., Vannucchi, P., 2004. Generic model of subduction erosion.
900   Geology 32, 913-916.
901   Weaver, S.D., Bradshaw, J.D., Laird, M.G., 1984. Geochemistry of Cambrian volcanics of
902   the Bowers Supergroup and implication for early Paleozoic tectonic evolution of
903   Northern Victoria Land Antarctica. Earth and Planetary Science Letters 68, 128-140.
904   Wilson, M., 1989. Igneous Petrogenesis. Unwin Hyman, London.
905

Figure 1
[Click here to download high resolution image](#)
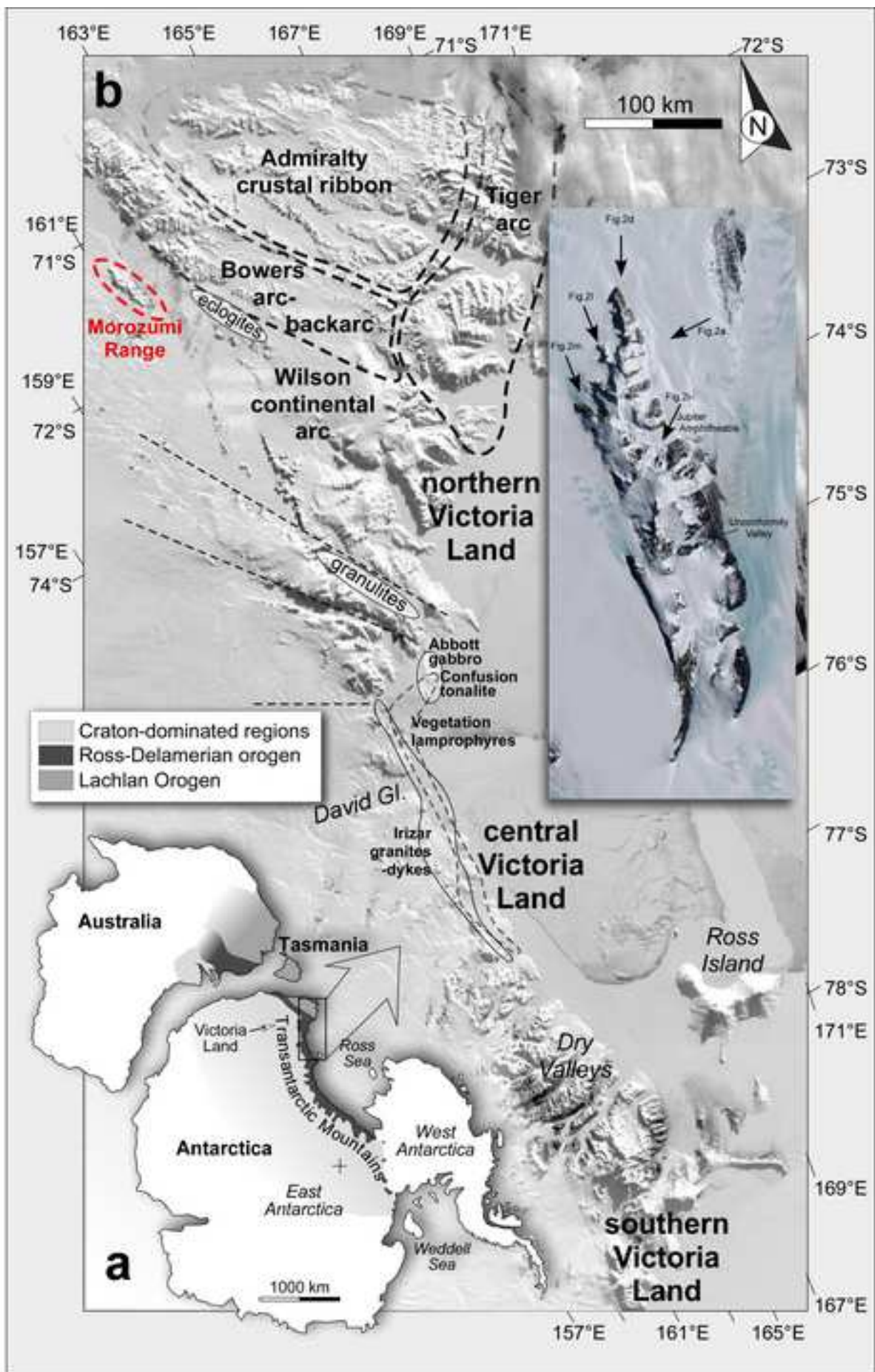
Figure 2
Click here to download high resolution image
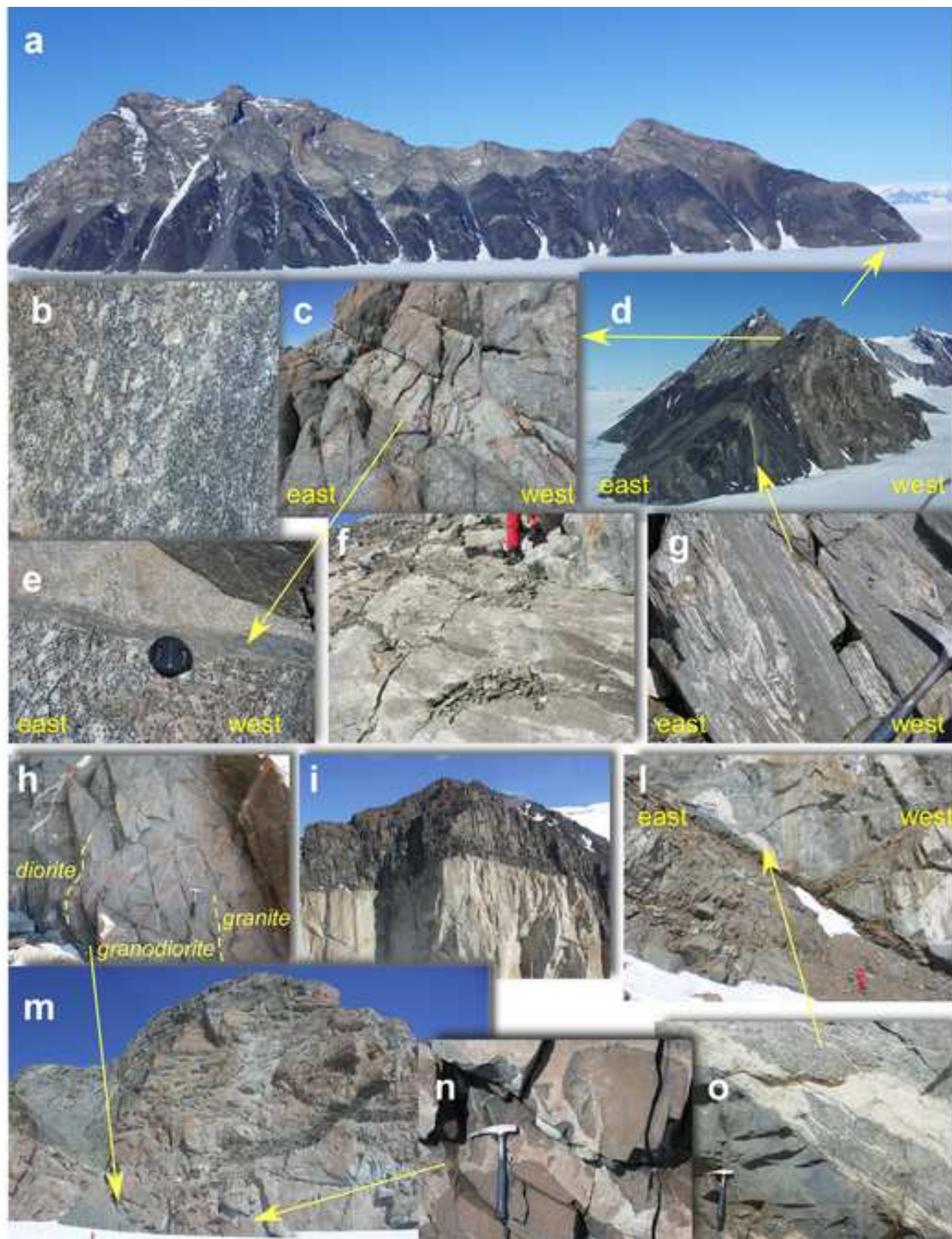
Figure 3
Click here to download high resolution image
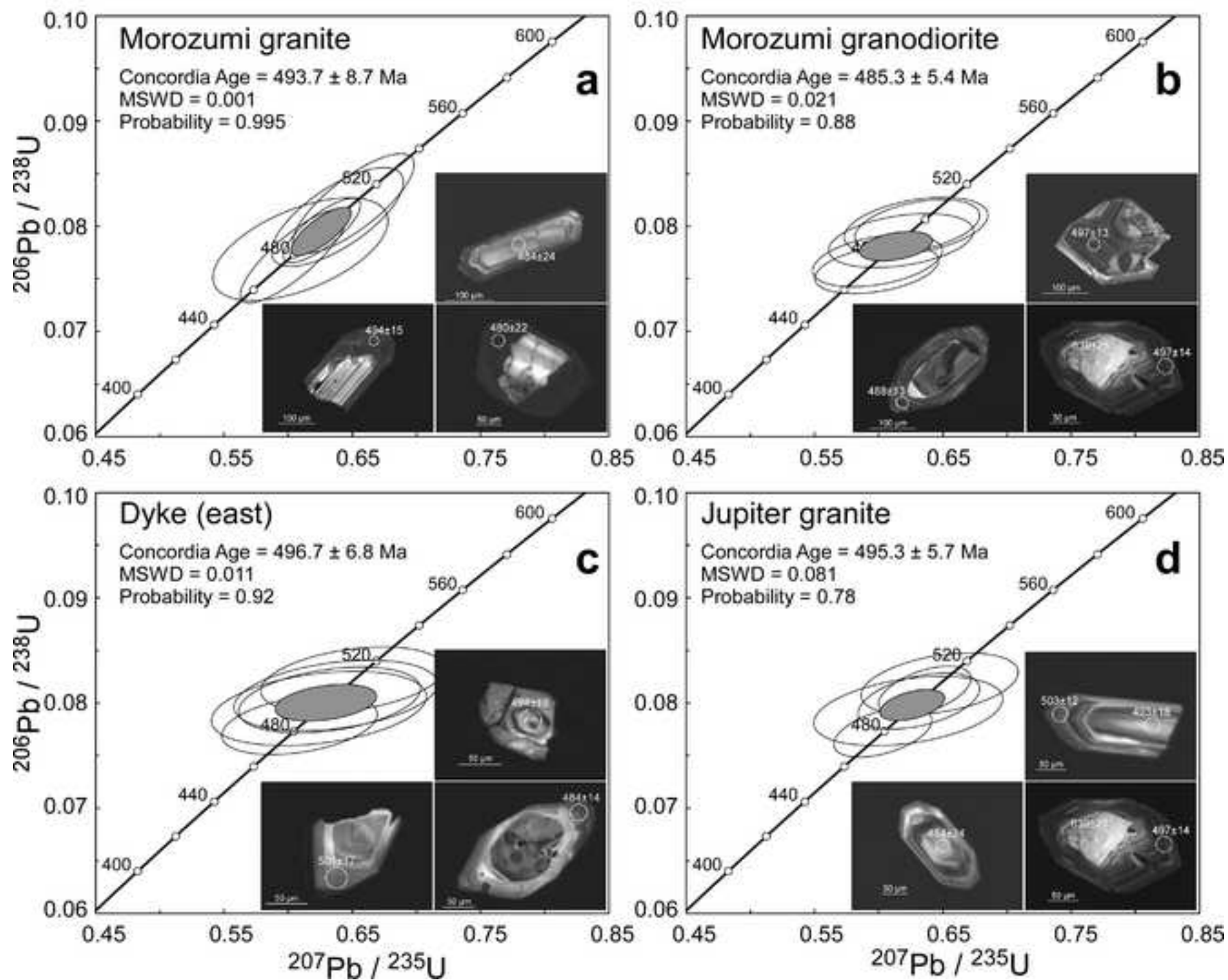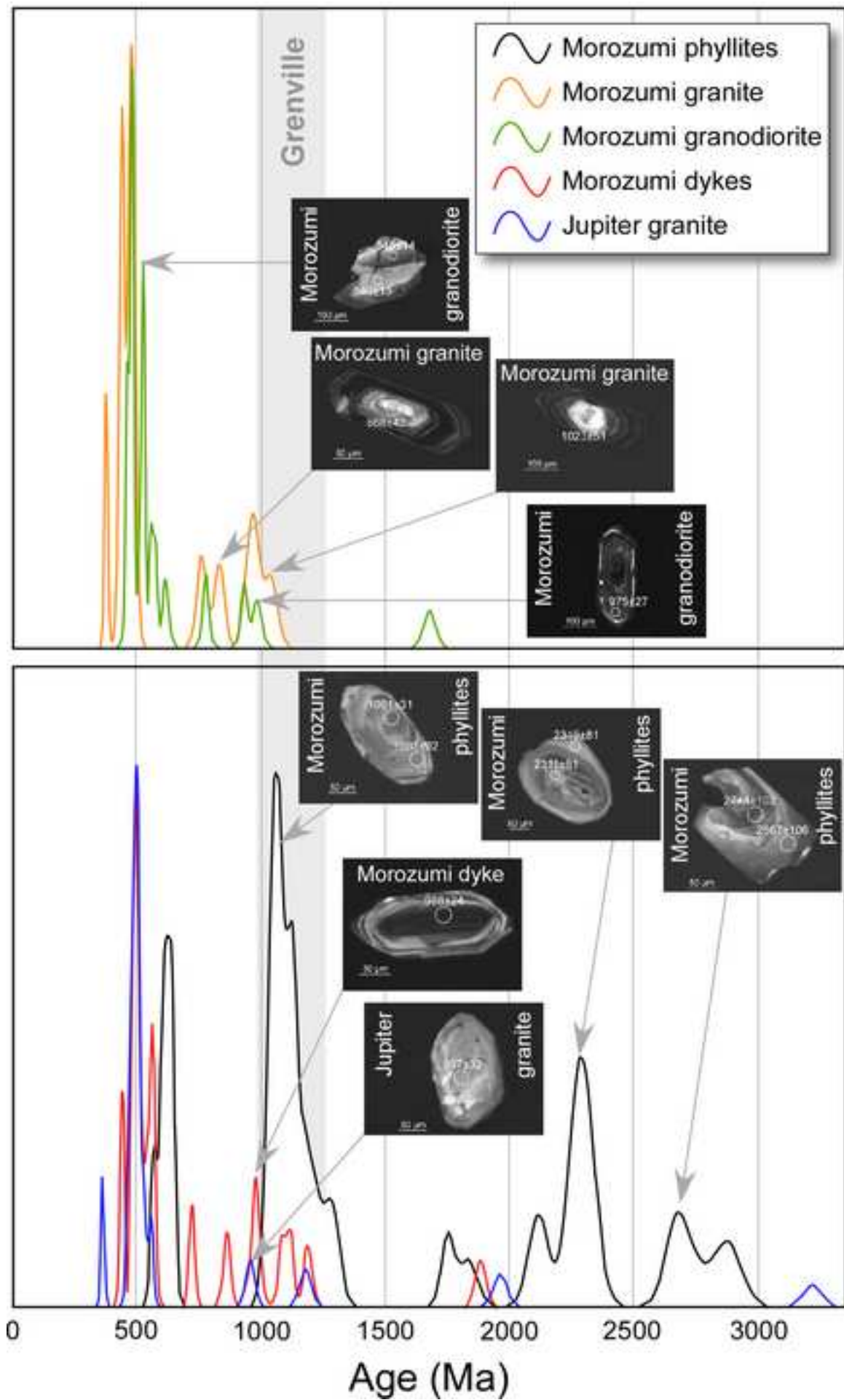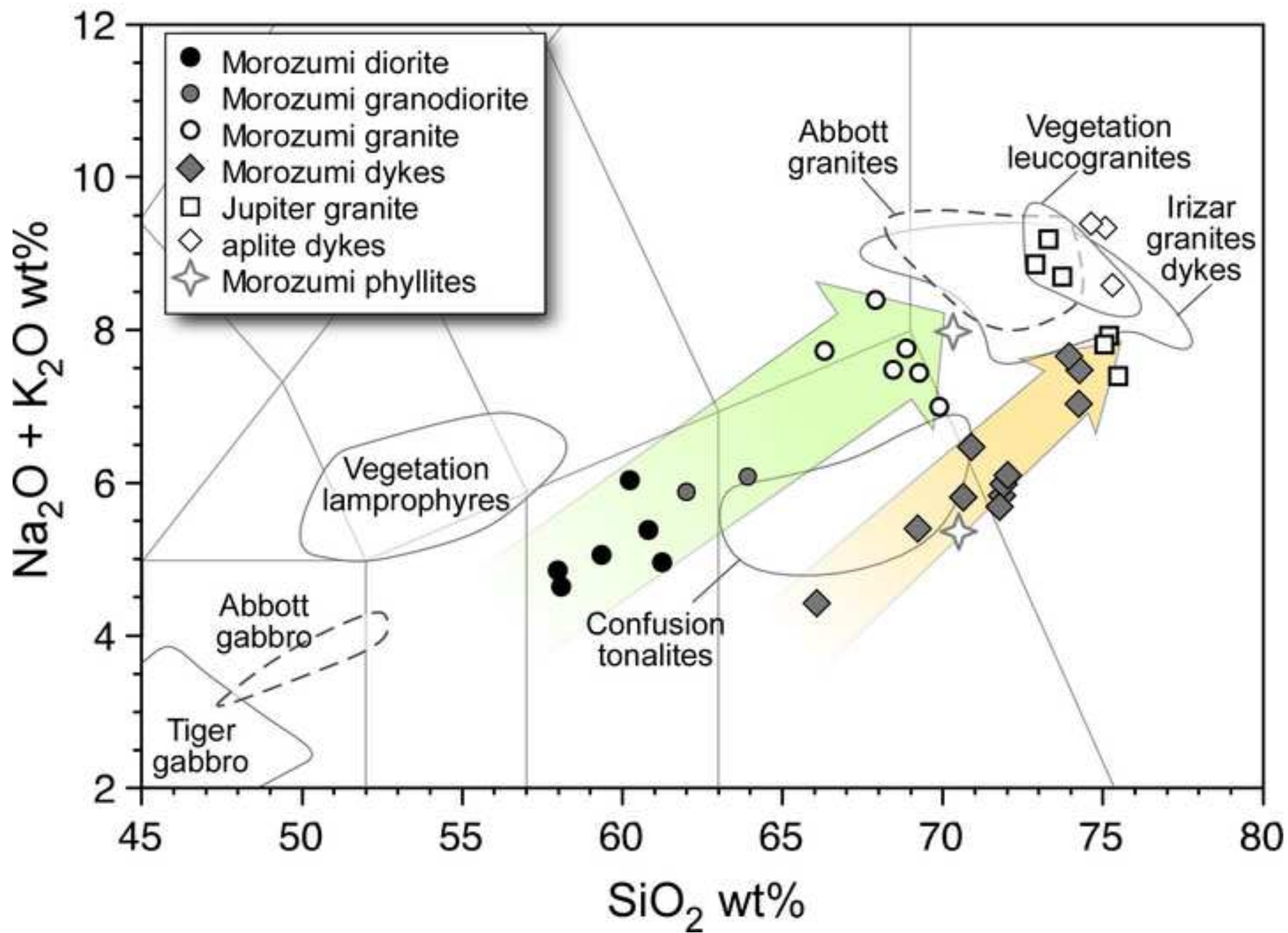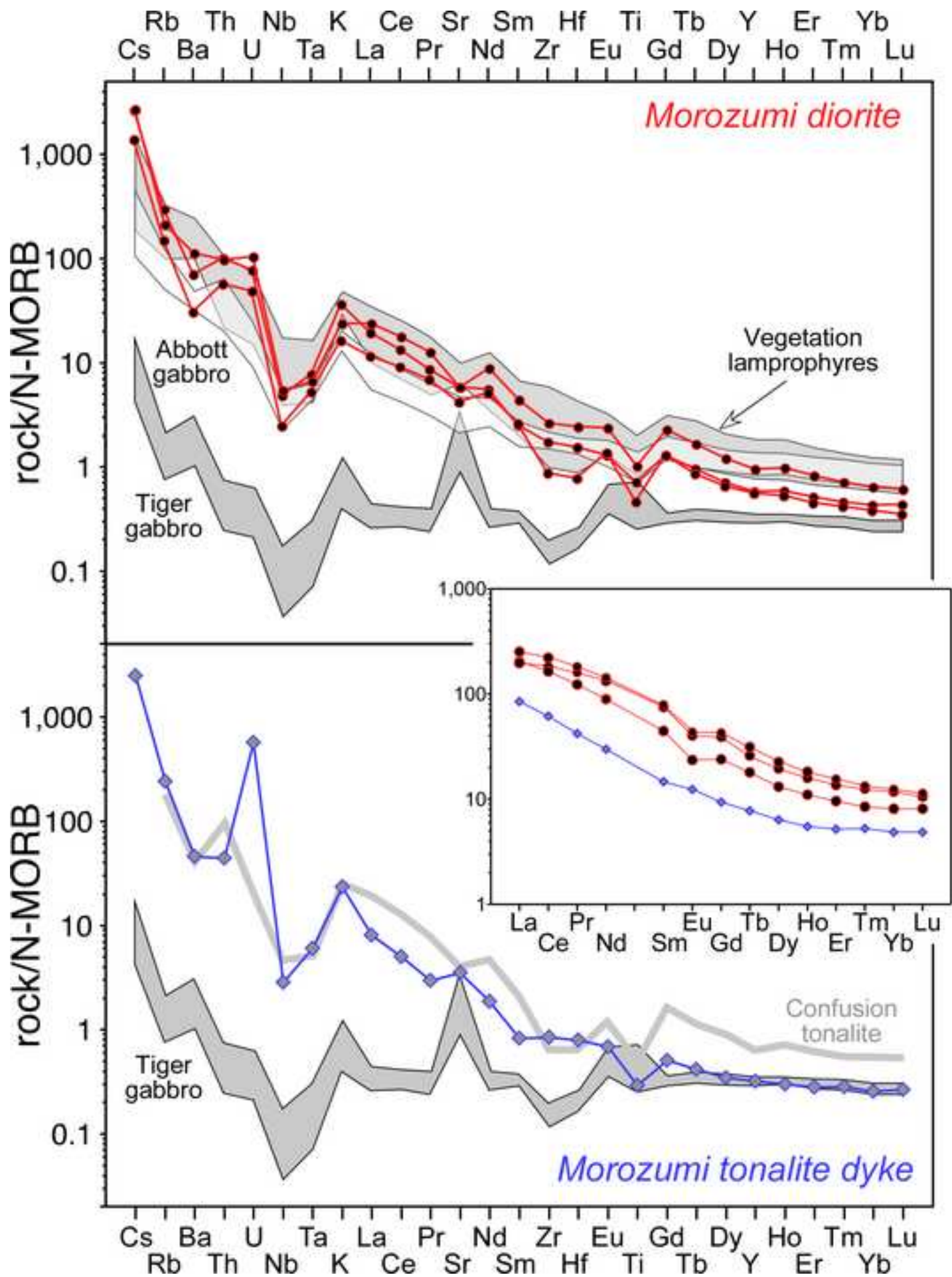
Figure 3

Figure 5

Figure 7
Click here to download high resolution image
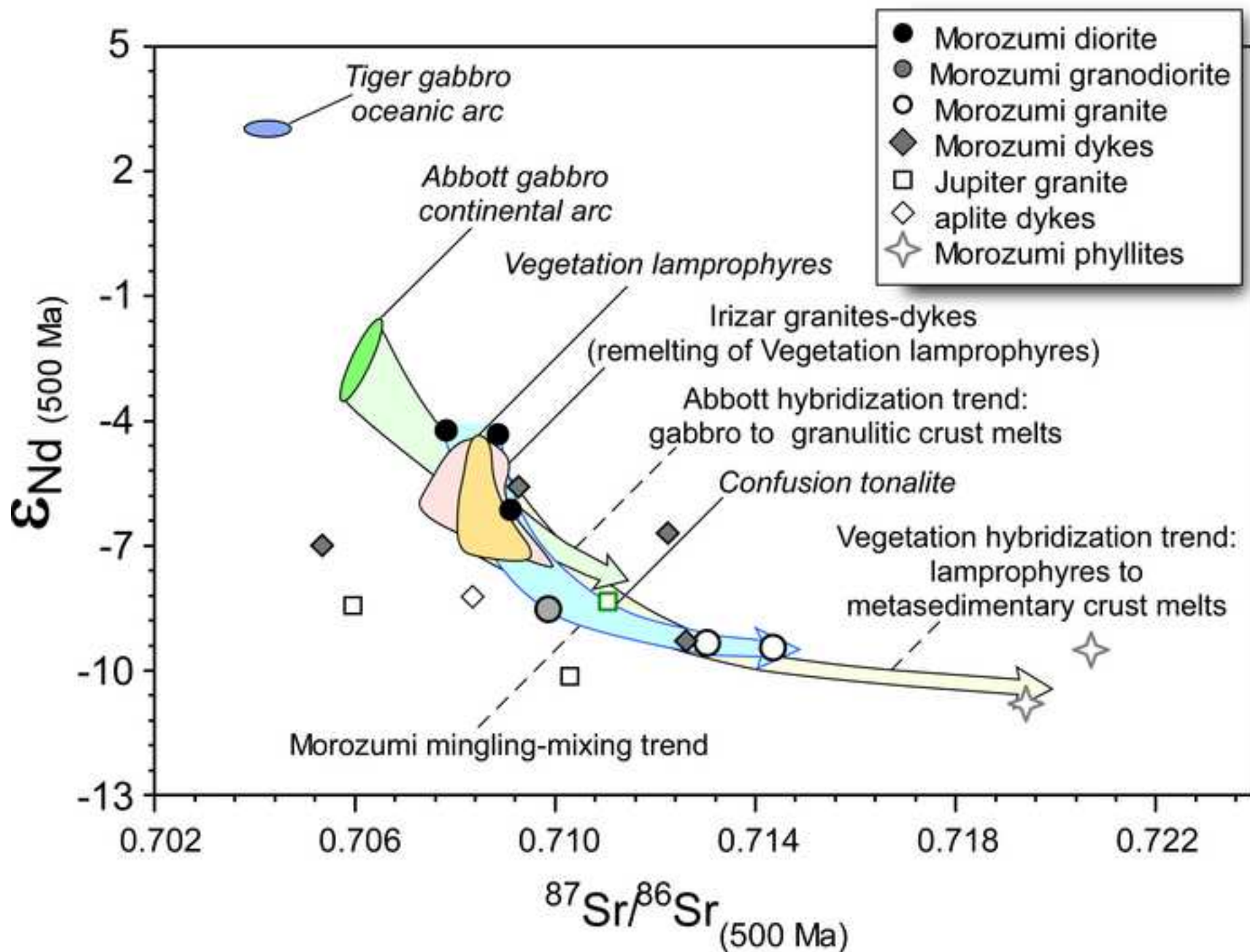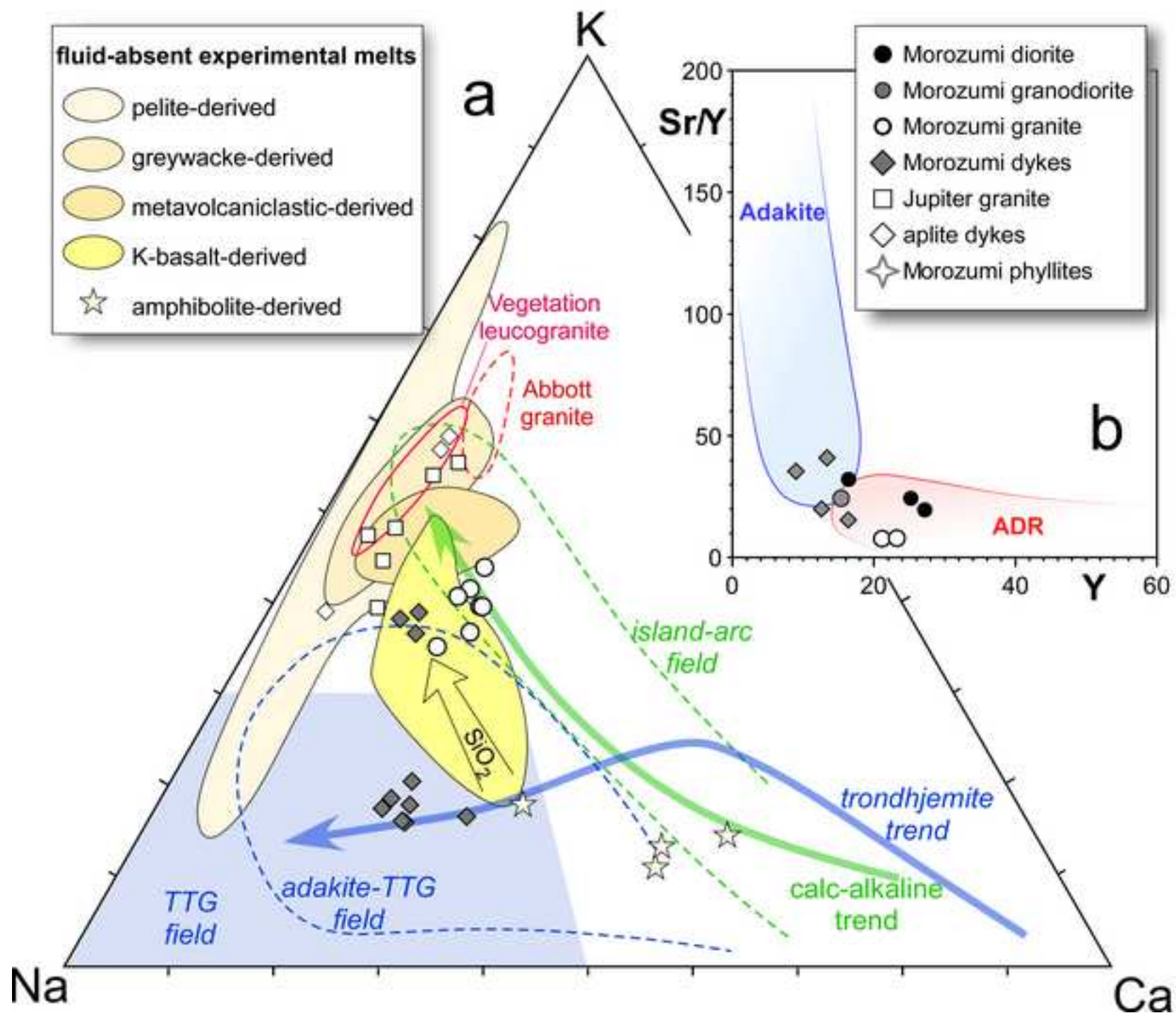
Figure 7

Figure 9
Click here to download high resolution image
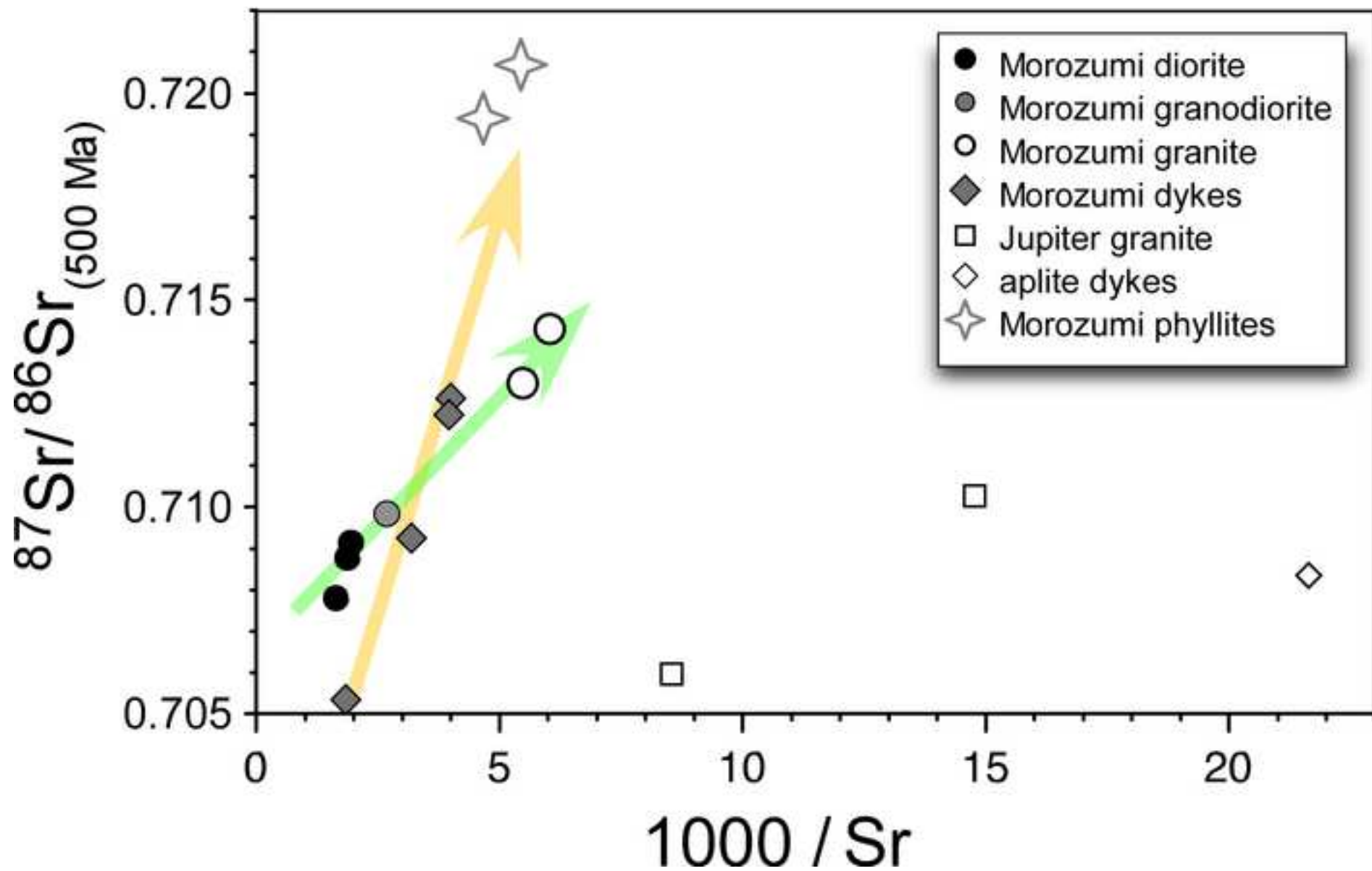
Figure 9

Figure 10
[Click here to download high resolution image](#)
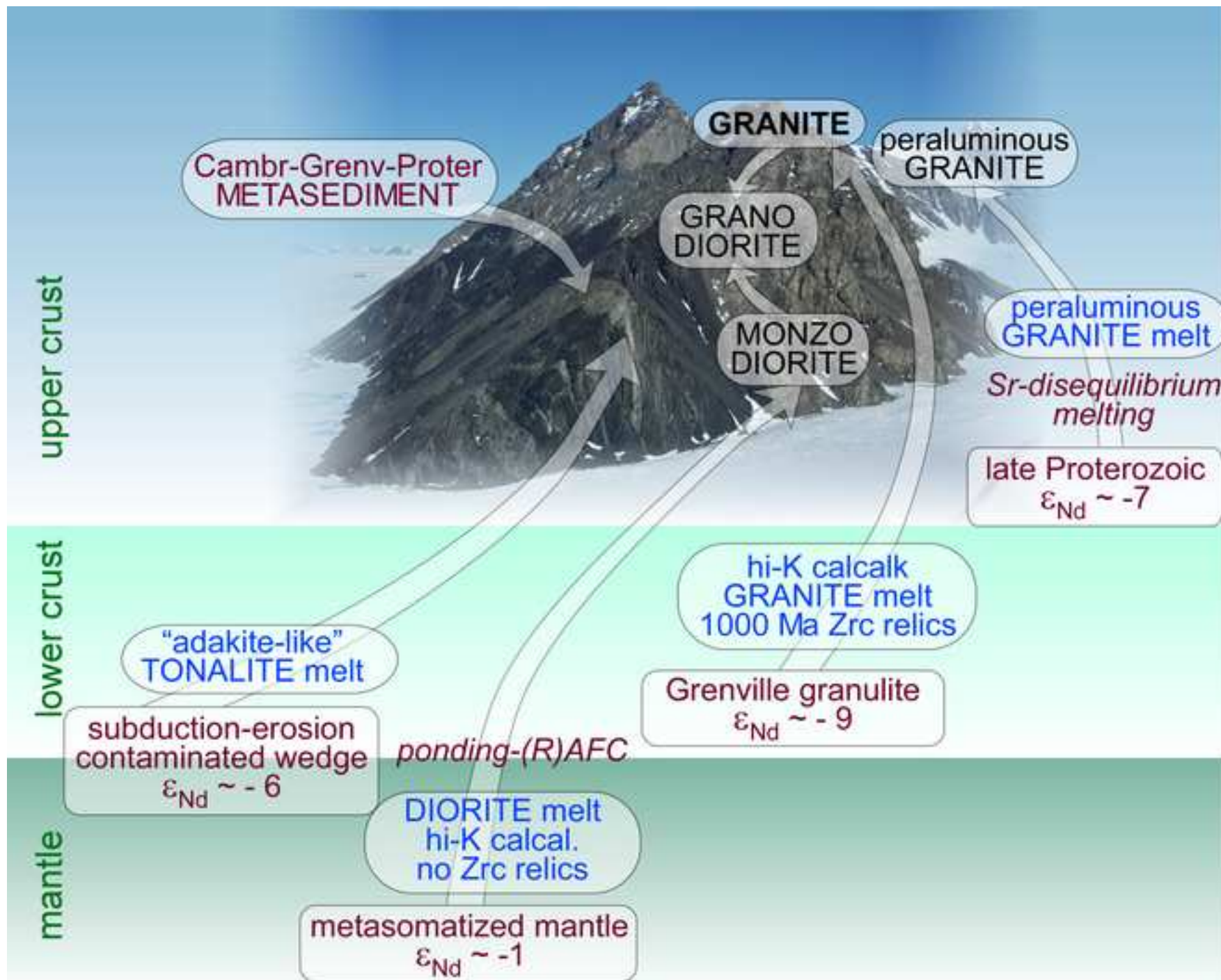
Figure 10

Labels within figure:

GRANITE

peraluminous GRANITE

Cambr-Grenv-Proter METASEDIMENT

GRANO DIORITE

MONZO DIORITE

peraluminous GRANITE melt

Sr-disequilibrium melting

late Proterozoic $\varepsilon_{Nd} \sim -7$

hi-K calcalk GRANITE melt 1000 Ma Zrc relics

"adakite-like" TONALITE melt

Grenville granulite $\varepsilon_{Nd} \sim -9$

subduction-erosion contaminated wedge $\varepsilon_{Nd} \sim -6$

ponding-(R)AFC

DIORITE melt hi-K calcal. no Zrc relics

metasomatized mantle $\varepsilon_{Nd} \sim -1$

upper crust

lower crust

mantle

Table 1. Summary of field, petrographic and geochronological features of the lithologic units of the Morozumi Range intrusive complex.

unit	sub-unit	rock type	petrography	structure	field chronology relative to Morozumi granite	age (Ma)
Morozumi phyllites				vertical foliation	earlier	
Morozumi granite		monzogranite	Kfs-phyric, medium-grained, bt-bearing	Kfs-phyric, vertical foliation		494 ± 9
Morozumi diorite		quartzdiorite	fine- to medium-grained, bt+amph-bearing	isotropic	coeval (hot, ductile contacts)	
Morozumi granodiorite		granodiorite	fine-grained	isotropic	coeval (diffuse contact)	485 ± 5
Morozumi dykes	eastern	tonalite-granodiorite	medium-grained, bt+ms-bearing	foliated	early-coeval (flattened)	497 ± 7
	western	tonalite-granodiorite	fine or medium-grained, bt±ms-bearing		late (crosscut granite foliation, ductile reationships)	
	crestal	leucomonzogranites - leucogranodiorites	bt±ms-bearing		post (crosscut granite foliation, brittle reationships)	
Jupiter granite		monzogranite	medium- to coarse-grained, leucocratic, bt+ms-bearing	isotropic	unknown	495 ± 6
Morozumi leucogranites/aplites		leucogranite	fine- to medium-grained, ms ± grt/tur-bearing		late	

Table 2. Major elements, trace elements and Sr-Nd isotopic data.

	Morozumi diorite						Mor. granodiorite		Morozumi granite						Morozumi phyllites	
unit																
sample	23.12.05 DS10	23.12.05 DS7	23.12.05 DS12	23.12.05 DS9	23.12.05 DS13	23.12.05 DS11	22.12.05 DS7	22.12.05 DS6	19.12.05 DS5	20.12.05 DS1	21.12.05 BS4	23.12.05 DS6	18.12.05 DS11	23.12.05 DS5	19.12.05 DS2	23.12.05 DS14
lat	71° 32.9'	71° 32.9'	71° 32.9'	71° 32.9'	71° 32.9'	71° 32.9'	71° 32.1	71° 32.1'	71° 27.08'	71° 26.9'	71° 28.3'	71° 32.9'	71° 29.9'	71° 32.2'	71° 46.8'	71° 33.2'
long	161° 37.7'	161° 37.7'	161° 37.7'	161° 37.7'	161° 37.7'	161° 37.7'	161° 38.7'	161° 38.7'	161° 42.0'	161° 49.9'	161° 44.3'	161° 37.7'	161° 44.9'	161° 43.0'	162° 10.9'	161° 47.8'
rock type	QD	QD	QD	MD	QMD	T	GD	GD	MG	MG	MG	MG	MG	MG		

Major elements (wt%)

	DS10	DS7	DS12	DS9	DS13	DS11	DS7	DS6	DS5	DS1	BS4	DS6	DS11	DS5	DS2	DS14
SiO_2	56.63	56.86	57.55	59.63	59.90	60.26	60.57	62.79	64.96	66.57	67.46	67.85	68.53	69.40	69.27	69.74
TiO_2	0.95	1.30	0.88	0.91	0.80	0.75	0.91	0.81	0.74	0.56	0.59	0.58	0.57	0.56	0.63	0.61
Al_2O_3	14.81	14.95	15.11	17.97	15.65	15.31	16.93	16.60	15.92	15.58	15.24	14.93	14.94	14.83	12.93	12.98
Fe_2O_3	6.82	8.52	6.52	6.10	5.88	5.84	5.88	5.19	4.62	3.19	3.80	3.71	3.52	3.58	4.01	5.36
MnO	0.11	0.13	0.09	0.09	0.09	0.10	0.07	0.07	0.07	0.06	0.07	0.06	0.06	0.06	0.05	0.07
MgO	6.32	4.82	5.46	3.04	4.80	5.17	2.76	2.30	1.51	1.13	1.22	1.23	1.16	1.17	2.18	2.68
CaO	6.81	6.22	6.22	4.92	5.84	5.84	4.54	4.27	2.27	2.59	2.64	2.40	2.64	2.59	1.36	2.02
Na_2O	2.85	2.84	2.81	3.33	3.06	2.90	2.97	3.01	3.09	3.01	2.99	3.01	2.98	3.04	1.69	2.83
K_2O	1.91	1.73	2.12	2.65	2.26	2.00	2.80	2.99	4.51	5.25	4.41	4.66	4.41	3.94	6.17	2.47
P_2O_5	0.53	0.60	0.31	0.36	0.29	0.31	0.36	0.29	0.34	0.18	0.21	0.19	0.20	0.20	0.20	0.16
LOI	1.96	1.97	1.87	1.78	1.66	1.58	1.40	1.99	1.99	0.87	1.17	0.88	0.69	1.18	1.07	1.18

Trace elements (ppm)

	DS10	DS7	DS12	DS9	DS13	DS11	DS7	DS6	DS5	DS1	BS4	DS6	DS11	DS5	DS2	DS14
Be	5.6	3.7	5.2				3.1					9.1	9.3		3.9	4.2
Sc	18.0	11.9	12.2				12.3					9.4	9.4		10.4	11.8
V	133.2	156.2	108.2				112.4					53.7	54.4		64.3	83.6
Cr	161.2	60.6	29.0				42.5					18.7	25.8		70.9	67.7
Co	26.7	24.8	15.6				15.2					7.2	7.4		10.0	12.3
Ni	124.7	38.9	19.1				26.1					8.6	7.9		26.5	31.1
Cu	36.9	20.3	51.5				34.8					10.9	19.7		5.0	32.0
Ga	18.4	17.7	21.3				21.8					19.8	19.3		15.9	17.3
Rb	134.6	119.6	165.5				165.0					260.4	244.4		185.5	142.4
Sr	610.6	526.0	528.1				373.8					183.0	165.7		214.6	183.8
Y	25.19	27.10	16.45				15.33					23.21	21.11		29.00	31.32
Zr	173	226	240				266					214	192			
Nb	9.33	12.75	11.42				12.91					15.92	16.31		12.72	13.10
Cs	15.64	19.06	18.60				7.53					24.69	44.92		18.35	11.76
Ba	312.3	714.9	444.0				501.5					526.5	543.1		845.2	318.9
La	46.82	59.75	48.36				61.94					58.40	46.14		50.24	31.51
Ce	110.65	135.24	100.74				129.26					123.03	97.21		102.58	65.61
Pr	14.79	16.82	11.48				14.83					14.20	11.26		11.94	7.80
Nd	60.46	65.42	40.87				53.16					50.28	40.49		44.10	29.21
Sm	11.13	11.70	6.61				8.45					9.25	7.54		7.99	6.12
Eu	2.27	2.43	1.33				1.32					1.27	1.27		1.36	1.13
Gd	7.76	8.51	4.75				5.76					6.55	5.51		6.36	5.37
Tb	0.94	1.13	0.65				0.70					0.88	0.78		0.94	0.83
Dy	4.81	5.57	3.23				3.20					4.53	3.92		5.20	5.04
Ho	0.87	1.00	0.60				0.56					0.83	0.75		1.03	1.07
Er	2.18	2.48	1.54				1.37					2.06	1.83		2.70	2.90
Tm	0.31	0.33	0.21				0.19					0.29	0.27		0.39	0.45
Yb	1.89	1.99	1.31				1.15					1.82	1.60		2.43	2.68
Lu	0.26	0.28	0.20				0.16					0.26	0.22		0.34	0.38
Hf	2.58	5.01	3.17				3.16					4.96	4.36		4.08	3.55
Ta	1.12	0.88	1.02				0.79					1.74	2.25		1.11	1.12
Tl	1.03	0.90	1.65				1.27					1.80	1.64		1.18	1.03
Pb	8.22	13.00	11.73				13.40					37.47	36.49		38.08	28.88
Th	10.98	11.73	12.06				17.11					27.04	20.76		17.90	11.90
U	3.69	4.93	3.63				1.24					4.41	2.56		2.32	2.76

Sr-Nd isotope data

	DS10	DS7	DS12	DS9	DS13	DS11	DS7	DS6	DS5	DS1	BS4	DS6	DS11	DS5	DS2	DS14
$^{87}Sr/^{86}Sr$	0.712345	0.713517	0.715543				0.718944					0.742427	0.744825		0.737277	0.736718
error (2s)	0.000070	0.000011	0.000011				0.000012					0.000012	0.000012		0.000010	0.000080
$^{87}Rb/^{86}Sr$	0.638	0.658	0.907				1.279					4.131	4.283		2.508	2.248
$^{87}Sr/^{86}Sr_{(500Ma)}$	0.707798	0.708826	0.709079				0.709833					0.712995	0.714309		0.719403	0.720700
$e_{Sr(500Ma)}$	55	70	73				84					129	148		220	238
$^{143}Nd/^{144}Nd$	0.512143	0.512130	0.512002				0.511873					0.511881	0.511880		0.511798	0.511922
error (2s)	0.000007	0.000007	0.000007				0.000006					0.000007	0.000005		0.000007	0.000007
$^{147}Sm/^{144}Nd$	0.1112	0.1081	0.0977				0.0961					0.1112	0.1126		0.1095	0.1266
$^{143}Nd/^{144}Nd_{(500)}$	0.511779	0.511776	0.511682				0.511558					0.511517	0.511511		0.511439	0.511507
$e_{Nd(500Ma)}$	-4.2	-4.3	-6.1				-8.5					-9.3	-9.4		-10.8	-9.5
T_{DM} (Ga)	1.55	1.55	1.68				1.85					1.91	1.92		2.01	1.92

Rock name abbreviations: D: diorite, MD: monzodiorite, QD: quartz diorite, QMD: quartz monzodiorite, T: tonalite, GD: granodiorite, MG: monzogranite, SG: syenogranite, AFG: alkali feldspar granite. Igneous rock names according to Q'-ANOR diagram after Streckeisen et al. (1978). T_{DM}: Nd model age calculated according to DePaolo et al. (1991)

Table 2 (ctd). Major elements, trace elements and Sr-Nd isotopic data.

unit	Mor. dykes-easterr		Morozumi dykes-western				Morozumi dykes-crestal					Jupiter granite					aplites-leucogranites			
sample	18.12.05 DS7	21.12.05 BS1	20.12.05 DS4	20.12.05 DS2	23.12.05 DS2	23.12.05 DS3	22.12.05 DS1m	21.12.05 BS7	21.12.05 BS5	22.12.05 DS1l	21.12.05 BS6	20.12.05 DS3	23.12.05 DS4	23.12.05 DS1	23.12.05 DS3	22.12.05 DS6	23.12.05 DS15	23.12.05 DS8	18.12.05 DS9	18.12.05 DS10
lat	71° 26.5'	71° 26.6'	71° 27.3'	71° 26.9'	71° 29.9'	71° 29.9'	71° 28.3'	71° 28.3'	71° 28.3'	71° 28.3'	71° 28.3'	71° 27.3'	71° 31.7'	71° 29.9'	71° 19.3'	71° 34.9'	71° 30.6'	71° 32.9'	71° 26.5'	71° 26.5'
long	161° 43.0'	161° 50.6'	161° 41.9'	161° 49.9'	161° 41.9'	161° 41.9'	161° 44.3'	161° 44.3'	161° 44.3'	161° 44.3'	161° 44.34'	161° 41.9'	161° 41.1'	161° 41.9'	161° 19.7'	161° 50.6'	161° 44.7'	161° 37.7'	161° 43.0'	161° 43.0'
rock type	GD	T	T	T	GD	T	GD	GD	MG	MG	MG	MG	SG	SG	SG	MG	SG	AFG	SG	SG
Major elements (wt%)																				
SiO_2	70.38	70.44	64.75	68.28	69.64	71.41	70.73	70.87	72.76	73.31	73.92	72.27	72.58	73.16	73.67	74.19	74.28	74.54	74.67	75.20
TiO_2	0.30	0.29	0.49	0.37	0.40	0.37	0.29	0.29	0.20	0.18	0.19	0.28	0.17	0.16	0.35	0.13	0.13	0.10	0.03	0.03
Al_2O_3	15.29	14.92	16.53	15.92	15.31	15.07	14.77	14.95	13.82	14.10	13.99	14.08	14.37	14.23	12.26	13.91	13.67	13.86	13.82	14.49
Fe_2O_3	2.61	2.53	4.48	3.41	3.25	2.99	2.72	2.86	1.79	1.50	1.69	1.68	1.25	1.29	2.41	1.23	1.33	0.97	0.48	0.31
MnO	0.05	0.05	0.08	0.06	0.05	0.04	0.04	0.05	0.03	0.03	0.03	0.04	0.03	0.02	0.04	0.04	0.05	0.03	0.01	0.06
MgO	1.26	0.95	2.47	1.44	1.08	0.93	0.84	0.76	0.60	0.50	0.56	0.61	0.36	0.55	0.76	0.30	0.36	0.24	0.14	0.11
CaO	2.86	3.02	4.76	3.70	2.92	2.93	2.70	2.79	1.80	1.83	1.60	1.31	0.97	1.12	0.86	1.19	0.98	0.73	1.04	0.69
Na_2O	4.48	4.07	1.90	3.63	3.92	4.02	4.07	3.82	3.20	3.35	3.40	2.59	3.25	2.92	2.24	3.34	3.24	3.74	2.60	4.12
K_2O	1.93	1.64	2.43	1.69	1.81	1.63	1.91	2.07	3.69	4.23	4.03	6.22	5.34	6.28	5.42	3.96	4.62	5.66	6.72	4.40
P_2O_5	0.11	0.10	0.10	0.11	0.17	0.10	0.12	0.11	0.09	0.10	0.10	0.14	0.20	0.14	0.10	0.08	0.18	0.08	0.08	0.10
LOI	1.21	1.66	2.25	1.19	0.93	0.78	1.17	0.96	1.23	1.50	1.09	1.24	0.86	1.27	0.95	1.61	1.04	0.89	0.79	0.94
Trace elements (ppm)																				
Be	3.1		3.2				4.3			5.5			7.3			10.6				6.3
Sc	6.5		7.1				5.7			4.2			3.4			5.3				2.5
V	36.7		41.2				22.1			10.5			7.2			9.4				0.6
Cr	32.6		36.1				10.0			7.3			6.8			5.7				4.7
Co	6.4		8.1				3.9			2.2			1.4			1.2				0.3
Ni	14.2		11.4				4.6			2.5			2.0			1.6				0.6
Cu	2.4		9.3				2.6			2.3			9.9			1.1				0.6
Ga	17.6		14.9				18.3			14.9			19.7			15.8				13.0
Rb	84.0		135.3				132.8			171.6			365.2			195.3				161.1
Sr	547.2		313.8				251.7			251.0			67.6			117.1				46.2
Y	13.41		8.94				12.59			16.34			13.12			25.13				12.40
Zr	133		122				143			99			87			72				28
Nb	5.79		6.63				15.66			10.07			17.16			11.23				7.12
Cs	8.95		17.25				8.68			5.88			20.48			17.03				4.85
Ba	406.3		288.5				212.6			660.1			213.7			405.8				248.9
La	21.16		20.11				28.22			29.86			22.76			16.48				5.68
Ce	42.83		37.60				54.40			57.03			49.34			34.65				12.41
Pr	4.87		3.90				5.93			6.17			5.74			4.07				1.46
Nd	18.11		13.61				20.54			21.10			20.61			15.00				5.43
Sm	3.73		2.17				3.43			3.80			4.70			3.29				1.78
Eu	0.66		0.70				0.76			0.80			0.54			0.60				0.16
Gd	3.18		1.87				2.74			3.02			3.70			3.08				1.64
Tb	0.49		0.28				0.40			0.46			0.54			0.58				0.32
Dy	2.47		1.57				2.16			2.55			2.63			3.60				1.89
Ho	0.46		0.30				0.41			0.53			0.42			0.80				0.39
Er	1.20		0.83				1.13			1.50			0.95			2.30				1.14
Tm	0.20		0.13				0.17			0.22			0.14			0.38				0.19
Yb	1.23		0.78				1.14			1.37			0.85			2.49				1.26
Lu	0.16		0.12				0.17			0.21			0.11			0.36				0.17
Hf	0.77		1.63				3.14			2.19			2.62			1.91				0.99
Ta	0.85		0.80				1.68			1.18			2.03			2.44				1.61
Tl	0.64		1.17				0.99			1.09			2.27			1.29				0.94
Pb	11.42		10.59				20.69			34.95			42.01			34.31				25.32
Th	6.98		5.26				8.86			10.98			12.84			8.14				1.91
U	0.62		26.50				2.24			2.63			3.72			2.96				1.37
Sr-Nd isotope data																				
$^{87}Sr/^{86}Sr$	0.708517		0.718166				0.723144			0.726733			0.822843			0.740428				0.780698
error (2s)	0.000009		0.000008				0.000011			0.000009			0.000011			0.000009				0.000010
$^{87}Rb/^{86}Sr$	0.444		1.249				1.529			1.982			15.801			4.842				10.157
$^{87}Sr/^{86}Sr_{(500Ma)}$	0.705351		0.709270				0.712250			0.712614			0.710254			0.705927				0.708328
$e_{Sr(500Ma)}$	20		76				118			124			90			29				63
$^{143}Nd/^{144}Nd$	0.512045		0.512023				0.511982			0.511873			0.511926			0.512000				0.512222
error (2s)	0.000007		0.000008				0.000007			0.000008			0.000009			0.000006				0.000009
$^{147}Sm/^{144}Nd$	0.1246		0.0965				0.1008			0.1089			0.1378			0.1325				0.1986
$^{143}Nd/^{144}Nd_{(500}$	0.511637		0.511707				0.511652			0.511516			0.511475			0.511566				0.511572
$e_{Nd(500Ma)}$	-7.0		-5.6				-6.7			-9.3			-10.1			-8.4				-8.2
T_{DM} (Ga)	1.75		1.65				1.73			1.91			1.96			1.84				1.84